Abstract

Colloidal particles at fluid interfaces: adsorption, assembly, and mechanics

Niveditha Samudrala

2017

Mechanics of emulsion droplets is crucial in applications where the encapsulated payload needs to be released under mechanical stimulus. This dissertation explores dumbbell nanoparticles as emulsifiers with focus on the emergent mechanical stability of the particle assembly at interfaces. Using a combination of freeze fracture shadow casting cryo-scanning electron microscopy and analytical modelling, I first investigate the complex adsorption behavior of individual dumbbells and discuss the corresponding implications for particle assembly at the interface. I then investigate the onset of mechanical instabilities in droplets stabilized by dumbbells using micropipette aspiration. I compare my findings to the control experiments of bare droplets and droplets stabilized with molecular surfactant under aspiration. In all three cases, the magnitude of the critical pressure for the onset of instabilities is set by the fluid surface tension. While particles have a dramatic impact on the mechanism of failure, the mechanical strength of the droplets is only modestly increased. This work provides experimental handles that can be tuned to aid the mechanical stability of emulsion droplets. The findings also inform advances in the mechanics of highly bendable sheets.

Colloidal particles at fluid interfaces: adsorption, assembly, and mechanics

A Dissertation
Presented to the Faculty of the Graduate School
of
Yale University
in Candidacy for the Degree of
Doctor of Philosophy

by
Niveditha Samudrala

Dissertation Director: Eric Robert Dufresne

May 2017

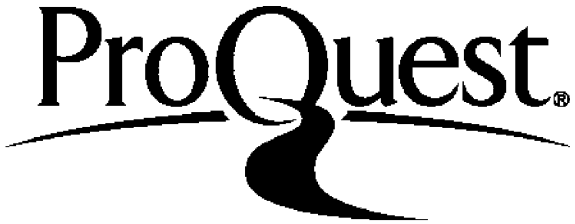

ProQuest LLC.
789 East Eisenhower Parkway
P.O. Box 1346
Ann Arbor, MI 48106 – 1346

Contents

List of Figures

Acknowledgements

I am forever in debt to my Ph.D. adviser, Eric Dufresne, who took me on as a graduate student during one of his busiest semesters at Yale. Eric has been invested in and vital for my growth as a scientist, communicator, teacher, and therefore, as a person. Among a gamut of precious experiences with Eric, I am most grateful for all the hours we spent designing experiments and deciphering data, his impromptu whiteboard lectures on soft matter in the lab, his carefully worded criticism that pushed me outside my comfort zone (for the better!), his empathy and calm during crises, and prep talks. I cannot thank you enough, Eric. So, I will instead persevere to make you proud by doing creative and thorough research that you continually inspire me to do.

I am grateful for the productive and exciting collaborations across two continents. Thank you, Jin Nam, currently a Senior Research Scientist at AmorePacific Co. in South Korea, for an exciting collaboration that defined and supported this thesis. Jin's pleasant disposition, technical expertise, and enthusiasm for experiments transformed his annual business trips to Yale into memorable learning experiences. Thank you, Lucio Isa, currently an Assistant Professor at ETH Zürich (Switzerland), for conducting all the FreSCa experiments reported in this thesis. Lucio's strong work ethic, quick turnaround time, and scientific rigor have truly made it a pleasure to collaborate.

I am thankful to my committee members: Eric Brown, Chinedum Osuji, and Corey O' Hern for their support, critical feedback, and friendly check-ins whenever I ran into them. I am particularly grateful for the Soft Matter class taught by Eric Brown, and Polymer Physics class taught by Chinedum Osuji. As someone who came in without any background in the field, I was glad to formally build my base in the fundamentals through their lectures, discussions, and problem sets.

Special thanks to Dr. Michael Rooks at the Yale Institute of Nano and Quantum Engineering (YINQE) for training me on the Scanning Electron Microscope and the Transmission Electron Microscope. I am also thankful to Mark Saltzmann and Elias Quijano for providing access to relevant lab equipment.

I have greatly benefited from discussing my project with John Wettlaufer, who was always generous with his time and helped me discover connections between seemingly different topics in science. I am also thankful to Dominic Vella and Mahesh Bandi, for their well-informed critiques on my project and for introducing me to theories in mechanics. All of them were also so kind to garnish their mathematical bent with some brilliant humor.

I am incredibly grateful to the team members at the Soft Matter Laboratory, who have traversed beyond their roles as colleagues to become friends, mentors, and siblings. The diversity of the lab, both intellectually and ethnically, fostered a healthy environment that nurtured science, ushered six o'clock sillies and many other fun moments, and challenged biases. In the order that I met them, I extend my heartfelt thanks and hugs to: Raph Sarfati, Ross Boltyanskiy, Aaron Mertz, Rob Style, Guy German, Chris MacMinn, Katie Rosowski, Callen Hyland, Anna von Berg, Kate Jensen, Qin Xu, Yingjie Xiang, Katrina Smith- Mannschott, Hendrik Spanke, and Mahi Ijavi. Special shout out to Raph, Ross, Aaron, Kate, and Mahi for their invaluable friendship, astute advice and opinions on a range of topics (including

science), their generosity with coffee, chocolate and hugs, long walks in New Haven and in Zürich, and many such seemingly small yet precious joys that made all the difference when the going got tough. Thank you!

Of course, the above list is incomplete as it does not include the many undergrads and Masters students whose brief stints in the lab added great value. I am grateful for my interactions with the lab alumni, who have been kind and welcoming to any questions I had. Thank you, one and all.

Special thanks to Sue Panella and Leslie Radcliffe at Yale, and Cornelia Aurelio at ETH Zürich for supporting the laboratory through their administrative wizardry.

I gratefully acknowledge the tremendous support from the School of Engineering and Applied Science (SEAS). SEAS administration, particularly Dean Vince Wilczynski and Cara Gibilisco, have been terrific in providing timely opportunities and resources, ensuring that I was successful, both at Yale and ETH Zürich. I am honored to be in the Advanced Graduate Leadership Program (AGLP) supported by SEAS. AGLP opened up fantastic avenues for professional development at the School of Management.

Outside the lab, I have had the good fortune of forging friendships with some of the nicest and smartest people at Yale. Amusingly, most of them also happen to be working in the labs of my committee members. Thank you, Gilad Kaufman, for all the valuable discussions about my project that helped me write a better thesis. Thank you, Kat Rokhlenko and Youngwoo Choo, for showing me relevant equipment and chemicals in the Osuji lab, graciously participating in Journal Club that I organized, and for the friendly chats in Mason. Thank you, Navneet Dogra, Nawal Quennoz, and Florian Carle, for your unfailing humor, delicious home-made meals, and Jenga stand-offs. Thank you, Manuel Mai and Airey Lau, for generously sharing your culinary exploits and for happily participating in my first triathlon.

I am also appreciative of all the wonderful times spent in New Haven with my friends: Alex and Ayinka Georgescu- Ambrose, Amanda Hoey, Anna Baron, Anup Rao, Coby Zeifman, Harish Prabhala, Jagan Padmanabhan, Neelima Sharma, Nidhi Pujara, Srikanth Toppaladoddi, and many others.

Special mention to Vikram Wali, Sre Muralidharan, Tomomi Sunayama, Sidzoo Singh, and Naruto Uzumaki for readily being there for me through the good and the rough patches of graduate school. One of them introduced me to the 3 Cs of life and all of them ensured that I fully embraced the 3 Cs regardless of my circumstances. You are all truly dear to me. Through your perspectives, patience, and perseverance, you have inspired me to be a better person, friend, intellectual, and therefore, a better scientist. Thank you!

Anyone who has spent quality time with me knows that I draw my strength, wisdom, and silly-ness from my partner, Siddharth Prabhu. He has been my strongest advocate, proudest ally, and wisest critic throughout the ups and downs of graduate school, and beyond. He is also the hardest to thank as words seem to fail in my attempts to articulate how indispensable his companionship has been to me. So, I will instead do my best to be as supportive of you, Sid, as you have been of me. I wish you the very best in life, and look forward to creating more amazing memories together.

Finally, I thank my family: amma and nana. They have continually nourished my roots with love and sensibility so that I could grow up aiming for the stars. They did their best to provide me with opportunities and resources that they never had and I am ever so grateful for all the sacrifices they made (happily) in the bargain. Their unquestionable confidence in me has made me responsible, independent, and resilient in life. I am incredibly blessed to have them for parents. If I have accomplished anything at all, I owe it to them.

Dedication

To my parents, Dr. Narahari Samudrala and Mrs. Sandhya Thota

Chapter 1

Introduction

1.1 Background and Context

An emulsion is a mixture of one immiscible fluid dispersed in another and stabilized against spontaneous phase separation using surfactants. Depending on the functionality of the emulsion, surfactants (or emulsifiers) can be protein complexes [22, 61], molecular surfactants [40, 41] , colloidal particles [84, 87], or microgels [13, 88].

Colloidal particles have been attractive emulsifiers for oil/water interfaces for the following reasons [11, 54, 55, 91]. First, they adsorb to the interface with high binding energies. The binding energy is given by $\Delta\ G = -\pi\ R^2\ \gamma_{ow}\ (1 - cos\ \theta_{ow})^2$, where R is the particle radius, γ_{ow} is the energy per unit area of the oil/water interface, and θ_{ow} is the contact angle as shown in Figure 1.1 (a) [5, 10, 11]. For 1 μm spherical particle equally wetting both oil and water ($\theta_{ow} = 90°$), the binding energy is on the order of $10^7\ k_BT$. Therefore, particles at an oil/water interface create a large kinetic barrier against mechanisms driving phase separation.

Particle adsorption to the interface is determined by surface tensions of the oil/water γ_{ow}, oil-particle γ_{op}, and water-particle interfaces γ_{wp}. These factors man-

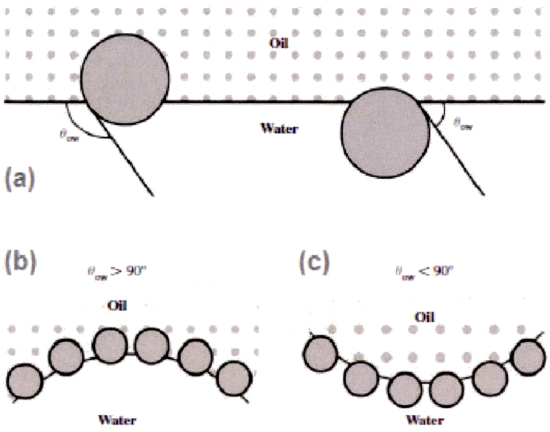

Figure 1.1: *Preferential wetting of particles* at (a) planar interface, (b - c) curved interface. "Lipophilic" particles form water-in-oil emulsions as shown in (b) while "hydrophilic" particles form oil-in-water emulsions as shown in (c). Figure has been reproduced from Ref. [11].

ifest through the contact angle θ_{ow}, which describes the equilibrium location of the particle at the interface. This is summarized by the Young-Dupré equation: $\gamma_{ow}\ cos\ \theta_{ow} + \gamma_{wp} = \gamma_{op}$. Particles equally wet by both liquids, $\gamma_{op} = \gamma_{wp}$, have $\theta_{ow} = 90°$. Particles preferentially wet by water ("hydrophilic"), $\gamma_{op} > \gamma_{wp}$, have $0° < \theta_{ow} < 90°$, while particles preferentially wet by oil ("lipophilic"), $\gamma_{op} < \gamma_{wp}$, have $90° < \theta_{ow} < 180°$. Depending on whether the particles are "hydrophilic" or "lipophilic", the resulting emulsion can be oil-in-water or water-in-oil as illustrated in Figure 1.1 (b-c) [11, 27]. Therefore, the contact angle of the particle determines wettability at the interface and the resulting interfacial curvature of emulsion droplets. Most importantly, θ_{ow} is experimentally accessible, tunable, and unique to the oil/water/particle system.

Second, colloidal particles at fluid interfaces open up new opportunities for assembling novel materials from bottom up. One strategy to do so is by *controlling particle parameters,* wherein intrinsic properties, such as shape, size, wettability, charge, and surface roughness are tuned to control how particles adsorb to the interface [27, 29, 40, 70]. Once adsorbed, the particle properties prompt specific inter-

particle interactions that drive the collective behavior of particles at the interface. For instance, particles that are anisotropic often deform the interface locally to maintain the three-phase contact line [12]. These interfacial deformations result in long-range capillary interactions that can drive particles into or away from assembling structures [12, 30, 57]. An additional instance is when particles adsorb to the oil/water interface from the oil phase. Surface charges on the particle play up image charge effects and electrostatics at the oil-water interface, driving the particles into ordered assemblies at the interface [53]. Another widely employed strategy is *molding and reconfiguring fluid interfaces* [15, 75]. Here, the curvature gradients in the interface serve as an external field to control the trajectories of the particles and amplify inter-particle interactions to achieve desired assemblies [15, 24].

Manipulating colloidal architectures at fluid interfaces can lead to novel optical [48, 59], catalytic [33, 35, 96], or mechanical properties [65]. Of particular interest in this thesis is the mechanics of particle-laden droplets.

Emulsions are often produced as a combination of shear, turbulence, and cavitation forces [91] but are deployed in applications where the encapsulated payload needs to be released under specific mechanical stimulus [68]. The mechanics of particle-laden interfaces also affect an emulsion's stability as they control the draining process during droplet coalescence [95], influence dessication of the droplet [80], and Ostwald ripening [63] [11]. Therefore, understanding mechanics of emulsion droplets is crucial for manufacturing [91], characterizing [60, 92], and deploying emulsions [68] that are stable and functional.

Mechanical properties of complex fluid interfaces are a subject of ongoing investigation [28]. Particle-laden droplets have been mechanically perturbed by squishing the droplet using force microscopy [26, 99], shearing the droplets by flowing them through confined channels [2, 46, 62, 69], changing the internal pressure of the droplet

by either applying osmotic shocks [18,19], tensiometry-like techniques [4,50] or drying the droplets [97,100], and applying electric field to deform the droplet [73,102]. Most of these studies report the importance of surface tension, interfacial elasticity, and the geometrical parameters of the emulsion in determining the mechanical stability. On the one hand, some results remain inconsistent, partly perhaps due to the sensitivity of the outcomes to the perturbation chosen. For instance, one study [86] reports that the ratio of particle size to drop size determines the order of magnitude of the measured "collapse pressure" while another study points out that the collapse pressure depends only on the droplet size and not the particle shape or size [98]. The latter study also states that single particle rearrangements impact the mechanical stability [98] while some studies report that particle-laden droplets buckle as jammed shells upon osmotic shock [18,19] leaving no room for rearrangements. On the other hand, a common thead tying coupled contributions from surface tension and shell elasticity exists across different perturbations [26,67,99,101,105]. For instance, the compression of particle-laden micrometric droplets using Scanning Force Microscopy [26] or Atomic Force Microscopy [99] reveals substantial deviations from the elastic shell models which are apparently contributions from surface tension. Similarly, the aspiration of sessile particle-laden millimetric droplets reveals buckling as the tension of the interface approaches zero [67,105]. Nevertheless, the exact roles played by surface tension and shell elasticity in determining the mechanics of particle-laden droplets remain unresolved.

1.2 Dissertation summary

In this dissertation, I adopt a bottom-up approach to study the mechanics of particle-laden droplets.

I use dumbbell-shaped nanoparticles as emulsifiers. In Chapter 2, I describe the synthesis of these particles using seeded-emulsion polymerization technique, which was developed by alumni of the Soft Matter Laboratory [79]. I then characterize the geometry, surface chemistry, and zeta potential of these particles to understand their intrinsic properties.

In collaboration with Dr. Lucio Isa at ETH Zürich, I first investigate the adsorption behavior of individual dumbbells to flat oil/water interfaces. In Chapter 3, we find that the dumbbells are surface active and adsorb to the interface in three different orientations. We directly measure the contact angles of the particles at the interface using freeze fracture shadow casting cryo- scanning electron microscopy (FreSCa cryo-SEM) . The dumbbells statistically express a preferred orientation that does not change for different wait times.

Based on our data, I hypothesize that this orientation is an equilibrium configuration defined by the contact angles of the individual lobes and the geometry of the particles. In Chapter 4, I develop a novel analytical model that treats dumbbells as two overlapping spheres. Using this model and additional mathematical arguments, I explain that the preferred orientation is indeed the equilibrium configuration. I further extend the model to predict different equilibrium orientations of particles at the interface based on the intrinsic parameters. I draw on our observations to develop a generalized model that could serve as a blueprint for designing interfacial assemblies.

I then investigate the mechanical stability of particle-laden droplets using mi-

cropipette aspiration. In Chapters 5 and 6, I focus on the onset of mechanical instabilities in these droplets. Dumbbell-laden droplets exhibit a two-step response to suction pressure, unlike the cases of bare droplets and droplets coated with molecular surfactant under aspiration. I show that while dumbbells have dramatic impact on the mechanism of failure, the mechanical strength of the droplets is only modestly increased. However, in all three cases, the magnitude of the critical pressures characterizing the onset of instabilities is set by the fluid surface tension.

I conclude with Chapter 7, where I explain our key findings and their impact on microencapsulation technologies applicable across several industrial sectors. I also explain opportunities for future work and make connections to current research on the mechanics of thin sheets.

Chapter 2

Synthesis and characterization of sub-micron amphiphilic dumbbells

J. Israelachvili defined two experimentally accesible variables for molecular surfactants that account for the physical and chemical forces in the system [40, 41]. The *packing parameter* accounts for the geometry of the surfactant as well as the dominant surface forces in the system. The *Hydrophilic-Liphophilic Balance (HLB) index* is given by the relative amounts of the hydrophilic and lipophilic components in the surfactant. Together, the packing parameter and HLB index can be used to predict the critical interfacial curvature and the interfacial microstructure. We hope to extend the phase space developed for molecular surfactants to colloidal particles.

Amphiphilic dumbbell-shaped nanoparticles can serve as colloidal mimics of molecular surfactants due to their geometrical and chemical anisotropy. By enhanced control over the particle's geometry and differential solvent affinity, we can manipulate the particles to achieve interfacial assembiles. However, bulk synthesizing non-spherical nanoparticles with high monodispersity is challenging. Surface tension dominates at lower length scales and favors spherical geometry.

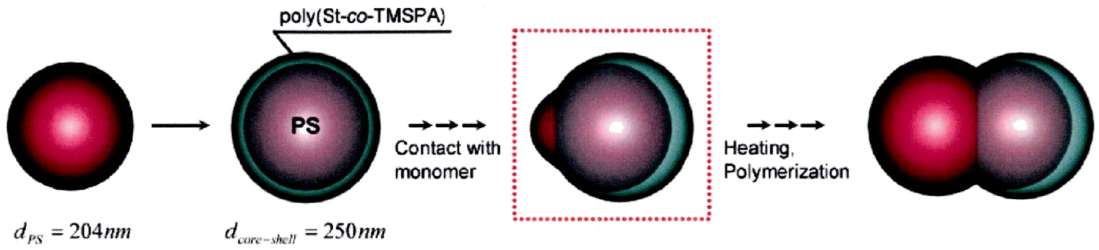

Figure 2.1: *Illustration.* Synthesis of dumbbell nanoparticles using seeded polymerization technique. Schematic has been reproduced from Ref. [79].

2.1 High-yield synthesis of monodisperse dumbbells

Previous efforts in the Soft Matter laboratory have successfully shaped a reliable high-yield route for making dumbbell polymer nanoparticles [79]. The method takes advantage of seeded suspension polymerization and involves three sequential steps as shown in Figure 2.1. First, monodisperse polystyrene nanospheres are synthesized to form the *core*. Next, a uniform hydrophilic shell composed of a random co-polymer of styrene and trimethoxysilylpropylacrylate (TMSPA) is grown around the core. Finally, the core is selectively swollen with styrene monomer to create an osmotic pressure imbalance. As a consequence, the core protrudes to form an additional lobe.

The extent of protrusion can be controlled with the relative volumes of swelling monomer and the core-shell as shown in Figure 2.2. Therefore, the synthesis described above can be used to make dumbbell-shaped nanoparticles in bulk with different packing parameters [41] as shown in Figure 2.1.

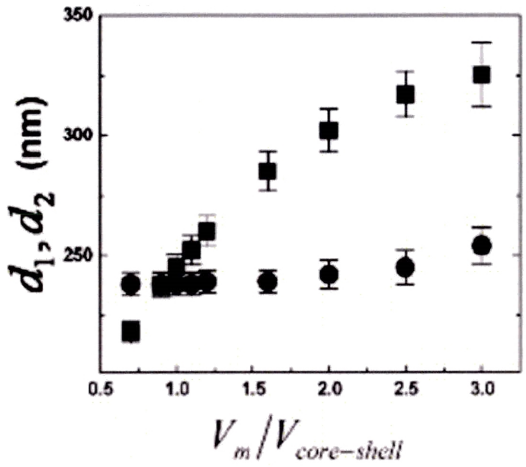

Figure 2.2: *Changing relative radii of dumbbells.* Dumbbells with different packing parameters can be synthesized by varying the relative volumes of swelling monomer to the core-shell. Graph has been reproduced from Ref. [79].

2.2 Characterization of particles

In this section, I will characterize the particles in terms of their size, surface chemistries, and zeta potential.

2.2.1 Particle size

I use the Scanning Electron Microscope (SEM) at the Yale Institute for Quantum and Nano Engineering (YINQE) to quantify the geometry of the particles and to attain statistics about the polydispersity in the bulk. The particles are thoroughly washed by centrifuging and resuspending in de-ionized (DI) water prior to imaging. A small volume of particles is squirted on the glass slide, attached to an SEM stub, and sputter coated with a few nm of Chromium prior to imaging in the SEM.

The dumbbells are typically synthesized with a major axis length of 500 nm. The radii of the two lobes can be independently varied between 200-300 nm as shown in Figure 2.3.

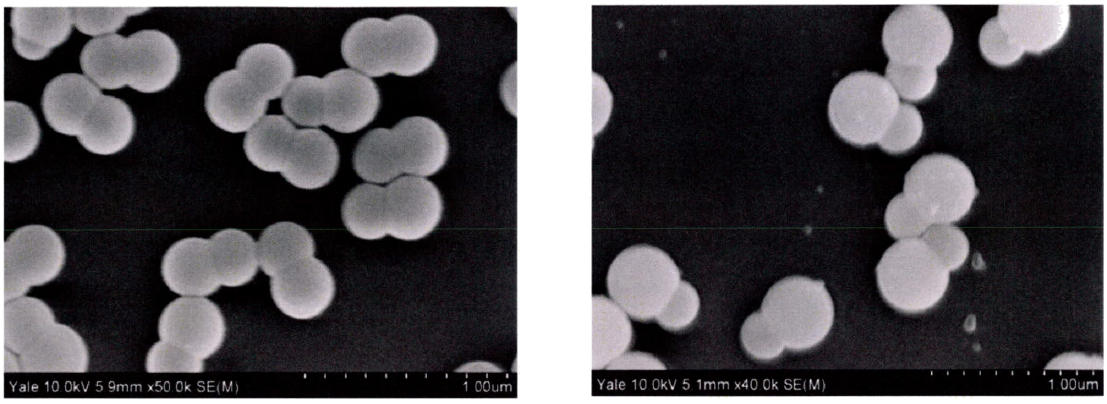

Figure 2.3: *Geometrical anisotropy in dumbbells.* Scanning Electron Microscopy (SEM) images of dumbbell-shaped particles synthesized with different geometrical anisotropies by controlling the relative volumes of monomer to core-shell. (Left) Symmetric particles where both lobes have equal radii (Right) Asymmetric particles, where the polystyrene lobe is smaller than the core-shell lobe.

Geometric Parameters: Aspect Ratio (AR) and α

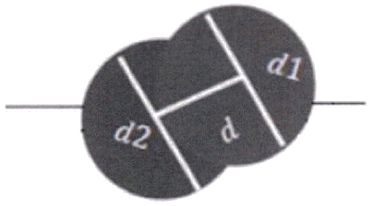

Figure 2.4: *Illustration.* Schematic of a dumbbell to define two important variables, Aspect Ratio (AR) and α.

I follow reference [78] and define two geometric parameters for upcoming chapters. If d_1 and d_2 are the diameters of the polystyrene lobe and the core-shell respectively, and d is the center-to-center distance between the two lobes as shown in Figure 2.4, then Aspect Ratio,

$$AR = \frac{d_1 + d_2 + 2d}{d_1 + d_2} \tag{2.1}$$

$$\alpha = \frac{d_1}{d_2} \tag{2.2}$$

Based on our current syntheses [79], I am able to achieve aspect ratio, $AR \in [1.5, 1.8]$ and relative lobe radii, $\alpha \in [0.5, 1.2]$.

2.2.2 Chemical heterogeneity

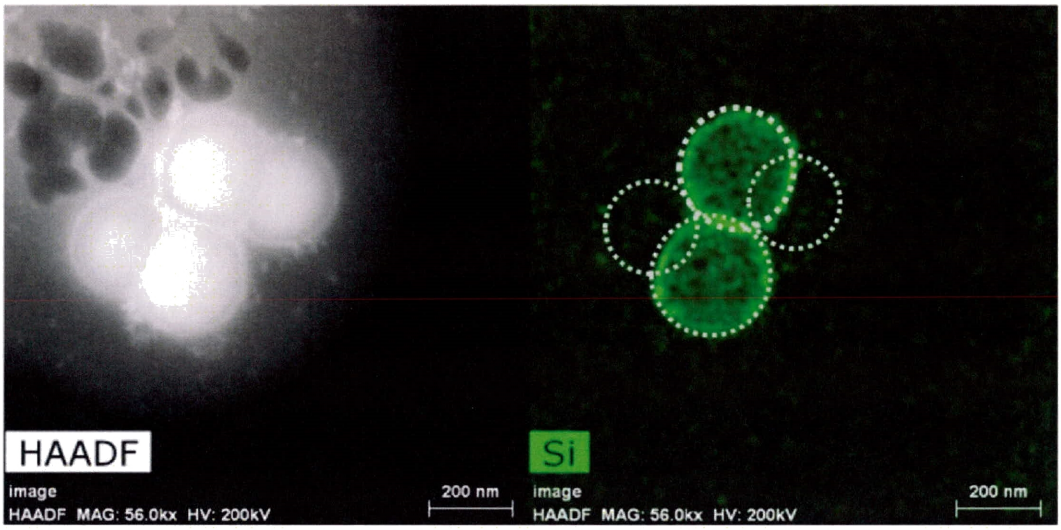

Figure 2.5: *Chemical anisotropy in dumbbells.* Images from Transmission Electron Microscopy in (left) high-angle annular dark field (HAADF) mode, and in (right) energy- dispersive X-ray mapping mode for Silicon as indicated in green. The dotted white circles are aides to the eye for identifying individual dumbbells shown in the HAADF mode.

With Dr. Michael Rooks, I characterize the chemical heterogeneity in the particles using high-angle annular dark-field imaging (HAADF) and energy-dispersive x-ray mapping on a FEI Tecnai Osiris 200kV Transmission Electron Microscopy (TEM) at the YINQE. Briefly, we impinge the sample with X-rays and map the peaks on the electromagnetic emission spectrum. The dumbell particles have putative polystyrene on one lobe and trimethoxy**sil**ypropylacrylate on the other. Therefore, Silicon (Si) in the TMSPA polymer is the distinguishing element between the two lobes since the other lobe is made of polystyrene alone. Use energy dispersive x-ray spectroscopy, we

map the location of silicon in the particles as shown in the right panel of Figure 2.5. We find that the Si is indeed localized to only one lobe, as indicated by concentration of green signal in Figure 2.5, confirming that the dumbbell surfaces are chemically anisotropic.

2.2.3 Electrokinetic stability

I use the Zetasizer Nano in Professor Mark Saltzmann's laboratory at the Department of Biomedical Engineering to quantify the zeta potential of the particles. Zeta potential, given by $|\zeta|$, is the electrokinetic potential in colloidal suspensions. $|\zeta|$ indicates the degree of electrostatic repulsion between adjacent, similarly charged particles in a dispersion and therefore, a key indicator of the stability of colloidal suspensions [41]. High zeta potential (positive or negative) indicates that the suspension resists aggregation while low zeta potential (positive or negative) indicates that the suspension may rapidly coagulate or flocculate. A rough dividing line between stable and unstable suspensions is generally taken at either +30 mV or -30 mV. The apparent zeta potential for our particles, as synthesized, is between -40 to -55 mV.

Depending on $|\zeta|$, electrostatics can dominate the interaction not only between particles but also between the particle and a bare oil/water interface. The surface charge at the oil/water interface has been argued to be negative and remains a controversial issue [8, 42, 89, 90]. Additionally, several studies in the literature discuss image charge effects on particle adsorption to oil/water interface. For instance, at certain pH concentrations, Behrens *et al* report experimental evidence that the electrostatic image force can hinder particle adsorption and emulsification even when the particle interaction with the interface charge is attractive [104]. Conversely, Chaikin *et al* report that,"even extremely hydrophobic, nonwetting particles can be strongly bound to like-charged oil/water interfaces because of image charge effects" [53].

Clearly, the literature in this domain is divided, making it essential to carefully study the $|\zeta|$ on colloidal particles. While investigating charges at oil/water interface or image charges is beyond the scope of this thesis, it is worthwhile to note that surface charges on the particles can have implications beyond stability of colloidal dispersions and affect emulsification.

Chapter 3

Adsorption of sub-micron amphiphilic dumbbells to fluid interfaces

A modified version of this chapter was published in *Langmuir* in 2014 [39]. The published work was co-authored with Lucio Isa and Eric R. Dufresne.

3.1 Introduction

Stabilization and control of fluid interfaces is the fundamental challenge in producing functional emulsions and foams. Droplets and bubbles are destabilized by surface tension, which drives their ripening and coalescence. Surfactants adsorb at fluid interfaces and improve their stability by either lowering the surface tension or creating a kinetic barrier to coalescence [11]. Molecular and macromolecular surfactants are technological workhorses of chemical, personal care, food, and pharmaceutical industries. Chemical engineers have exquisite control of their geometry and differen-

tial affinity for solvents, which enables their application to a wide array of materials and scenarios [41]. However, micro and nanoparticle-based surfactants have a much higher binding energy to fluid interfaces and are a desirable alternative when more stable and tougher emulsions are needed [5, 11, 23]. Until recently, surface-active particles have come in limited geometries and chemical compositions. The structure of Janus and patchy colloidal particles mimics the flexibility of molecular surfactants, with robust control of geometry and differential solvent affinity [51]. Janus and patchy spheres are typically functionalized on a flat surface, and therefore very difficult to produce at scale [43, 81–83]. Alternatively, bulk-synthesized amphiphilic particles are a promising scalable alternative [58, 79].

In order to understand the efficacy of amphiphilic micro and nanoparticles at stabilizing fluid interfaces, we need to first understand the kinetics and energetics of how they adsorb to a fluid interface. Recently, Lee *et al* used a Metropolis Monte Carlo simulation to calculate binding energies and equilibrium orientations for a wide variety of particle geometries and compositions [77, 78]. They considered bifunctional particles with polar and apolar patches in a variety of geometries including spheres, ellipses, and dumbbells. The polar and apolar lobes are characterized by their equilibrium contact angles with the fluid interface, θ_p and θ_a, respectively. For each particle type, they determined the binding energy, position, and orientation at the interface. This approach has recently been confirmed by careful measurements of the geometry of adsorbed millimeter-scale particles at a fluid interface [74]. Applications involving the stabilization of fluid interfaces call for an extension of these results to technologically relevant micro and nanoparticles.

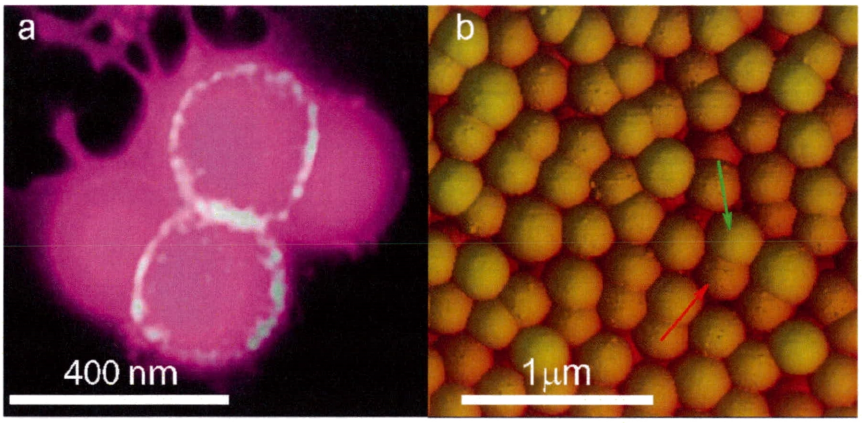

Figure 3.1: *Identifying polar and apolar lobes from micrographs.* (a) Transmission Electron Micrograph (TEM) of polymer dumbbell particles from batch A. The TEM dark field image is in purple, and the energy-dispersive X-ray map for Silicon (Si) is superimposed in white. The *polar* lobe shows Si. The *apolar* does not contain Si, and therefore, no representative white signal. (b) Atomic Force Micrograph (AFM) of polymer dumbbell particles (batch A). The arrows highlight the *polar* (red) and *apolar* (green) lobes. The polar lobes show higher surface roughness.

3.2 Materials and Methods

3.2.1 Dumbbell particles.

These particles were synthesized as described in the previous chapter, and are composed of polystyrene and poly(styrene-co-trimethoxysilylpropylacrylate) lobes . The surface of the dumbbells was imaged by Atomic Force Microscopy in tapping mode on a Bruker Dimension with a silicon cantilever (26 N/m, 300 kHz, Olympus). In addition to the different chemical composition, the two lobes also present a different surface roughness, as shown in the AFM image of Figure 3.1 b.

Based on the chemical composition, we expect the polystyrene lobe to be close to neutrally wetting (contact angle around 90°) and the poly-(styrene-co-TMSPA) lobe to be relatively "hydrophilic". In order to keep our arguments general for any kind of wettability contrast between the two lobes, for the rest of this work, we will refer to the polystyrene and poly-(styrene-co-TMSPA) lobes as the *apolar* and *polar* lobes respectively. Note that polar lobe is always rougher than the apolar, and this may be due to partial phase separation of the TMSPA from the PS during synthesis.

Particle type	R_p(nm)	R_a(nm)	AR	$\alpha = R_a/R_p$	# particles
A	136±6	147±7	1.7±0.1	1.1±0.1	100
B	148±5	124±6	1.7±0.1	0.9±0.1	128
C	159±7	126±16	1.7±0.1	0.8±0.1	149

Table 3.1: Dimensions of dumbbell particles from conventional SEM images. The error bars are the standard deviations in the distributions

For this investigation, we considered three batches of particles with slightly different sizes and shapes. The geometries of these particles are characterized with SEM and summarized in Table 3.1.

All three batches of particles have similar aspect ratios, AR $\approx$ 1.7. The batches have more variation in their relative size, α, which ranges from 0.8 to 1.1, as shown in Table 3.1.

Note: For the sake of clarity, I will lead this chapter using data from Batch A. The data for Batches B and C are available online in the Supplementary Information of Ref. [39].

3.2.2 Freeze fracture shadow casting cryo-scanning electron microscopy (FreSCa cryo-SEM)

We use FreSCa cryo-SEM to characterize the adsorption of dumbbells at an n-decane/water interface [38]. This technique surpasses several limitations involving contact angle measurements of nanoparticles by directly visualizing the particles at the interface, [37,38]. The technique developed by L. Isa *et al* has been used to measure contact angles of amidine latex particles of 20 nm diameter with single particle resolution and measurement error as low as few degrees [37,38].

Figure 3.2 summarizes sample preparation and imaging strategy. As shown in Figure 3.2 (a), an oil/water interface is created, with dumbbells suspended in the water phase. The dumbells adsorb to the interface due to their surface-active nature

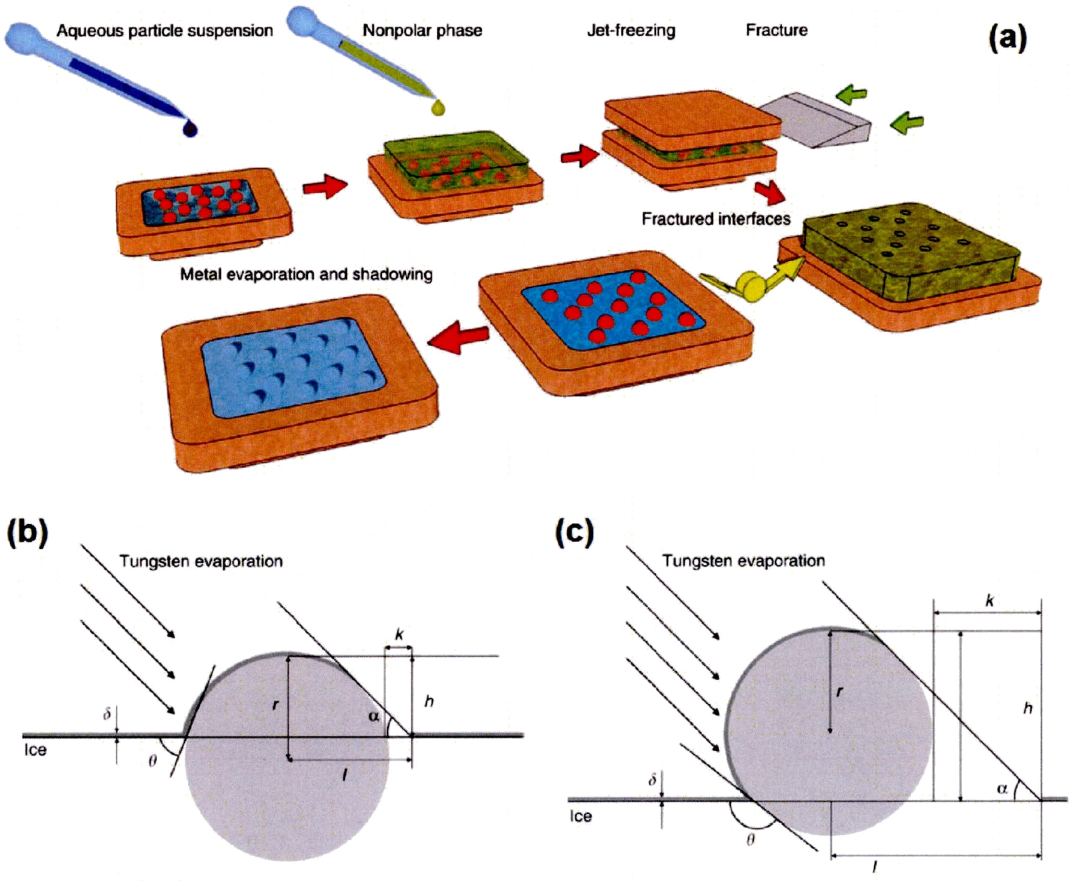

Figure 3.2: *Sample preparation protocol for FreSCa cryo-SEM.* (a) Scheme of the sample preparation for FreSCa cryo-SEM imaging. Representation of (b) hydrophilic and (c) hydrophobic nanoparticle of radius r at the vitrified water interface after metal evaporation. The three-phase contact angle θ, the metal deposition angle α and thickness δ, the height of the particle relative to the interface h, its projection along the metal deposition direction l, and the length of the shadow k are highlighted. Figure has been reproduced from Ref. [38]

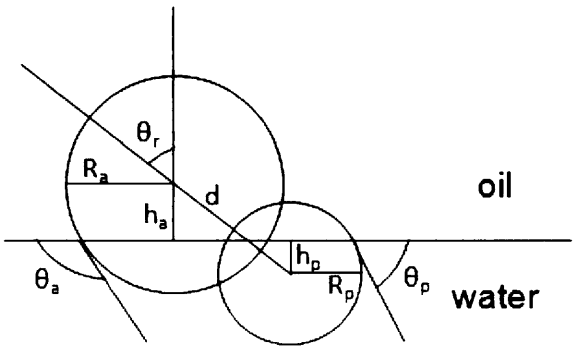

Figure 3.3: *Illustration.* Schematic highlighting the geometry of the dumbbells at the fluid/fluid interface.

and remain trapped given the lack of any external energy for desorption. The sample is then jet-frozen from room temperature to -140° C at the rate of 30,000 K/s, in order to prevent water crystallization, following which the sample is fractured at -140° C. The interface acts a weak fracture plane resulting in preferential fracturing along the interface. The oil phase is discarded and the vitreous water phase having a fraction of the trapped particles is utilized for imaging and analyses.

The vitreous water phase is unidirectionally coated with Tungsten for a preset thickness δ at a known angle α as shown in Figures 3.2 (b-c). This coating results in a noticeable surface contrast during SEM imaging. Based on calculations in [38], we can estimate the particle's penetration length and deduce the contact angle (see Figure 3.3).

The contact angle, θ_i, is given by simple trignometric relations that correlate the lobe cross-section, shadow length (both obtained from SEM images) and particle radius (known) as follows,

$$cos\ \theta_i = \frac{|h_i - R_i|}{R_i}, \tag{3.1}$$

where $i \in \{a, p\}$ and (h_a, R_a), (h_p, R_p) are the heights of the lobe center relative to the interface and radii for the apolar and polar lobes, respectively.

Additionally, we also define the angle θ_r, as the rotation angle of the dumbbell axis relative to the normal to the interface as follows,

$$\theta_r = cos^{-1}\Big[\frac{h_a + h_p}{\sqrt{(x_a - x_p)^2 + (y_a - y_p)^2 + (h_a + h_p)^2}}\Big], \tag{3.2}$$

For our measurements, the interface was coated with tungsten at 30° angle, which casts shadows encoding the positions of the particles relative to the interface [38].

3.3 Dumbbells have a preferred orientation at the interface

A typical FreSCa image of dumbbells adsorbed at the interface is shown in Figure 3.4. This figure shows particles supported by vitrified water after the removal of the oil phase. Three populations of particles are visible. For the majority of particles, both the polar and apolar lobes intersect the interface (e.g., particle number 8 in Figure 3.4). The rest of the particles have only one of the two lobes in contact with the fluid interface. For example, particles 28 and 33 in Figure 3.4 contact the interface with only the polar and apolar lobe respectively. These three geometries are shown schematically in Figure 3.5 a.

We counted the number of occurrences of each orientation for all three particle types, as reported in Figure 3.5 b. Here, the aqueous subphase was vitrified 10 s after the creation of the oil/water interface. Configuration I, where both lobes intersect the interface, was strongly preferred. Configuration II, where only the polar lobe touches the interface, was second. Configuration III, where only the apolar lobe intersects the interface, was least likely.

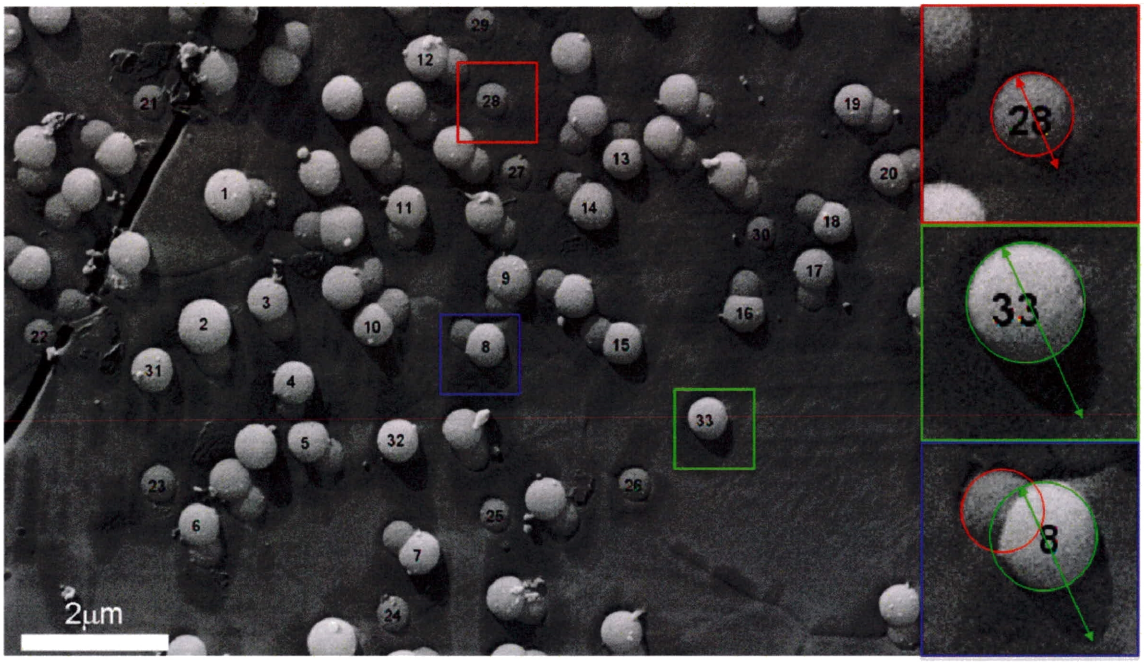

Figure 3.4: *Representative FreSCa cryo-SEM images of sample A vitrified after 10 s.* The particles in the image are embedded in vitrified water, and the n-decane has been removed by fracture. Due to the different materials of the two lobes, see Figure 3.1 a, the polar lobe appears slightly darker than the apolar lobe. Each particle suitable for contact angle measurement (e.g., distance between particles larger than shadow length) is numbered and the relevant quantities are measured. The three particle populations are visible. One example of each type is zoomed in and visualized on the right. (Top right) Particle for which only the polar lobe is visible at the interface. Here we measured the size of the particle cross-section at the interface and the shadow length and used these values to calculate the contact angle and size. (Middle right) Particle for which only the apolar lobe is visible. Here we measure the contact angle and the size. (Bottom right) Dumbbell particle where both lobes intersect the interface. For the apolar lobe, we use the same procedure as for particle 33; while for the polar lobe, we fit its cross-section to a circle to measure the contact angle by comparing the former with the average lobe size measured separately by conventional SEM.

a

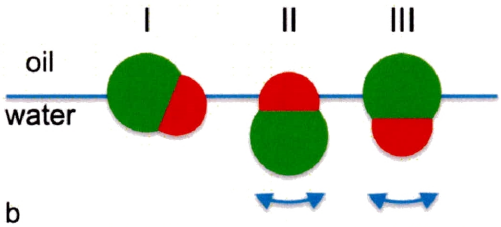

b

	I	II	III
Batch A (N=801)	78%	17%	5%
Batch B (N=235)	64%	30%	6%
Batch C (N=1441)	60%	38%	2%

c

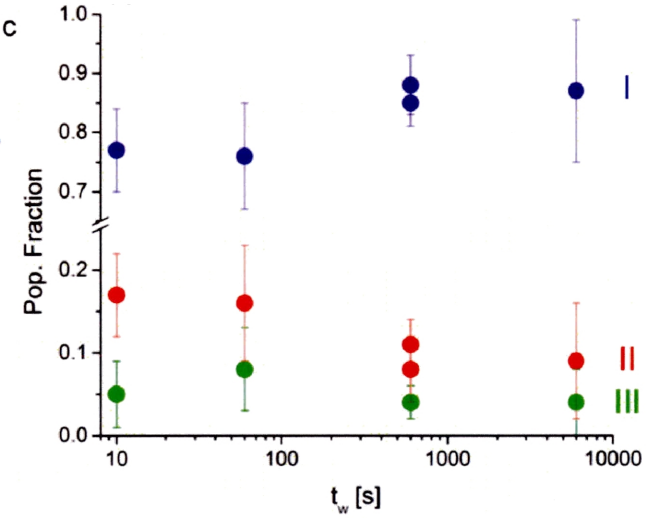

Figure 3.5: *Summary of orientation data across different batches of particles.* (a) Schematic showing the three observed orientations of dumbbells at the oil/water interface. The green lobe is apolar and the red lobe is polar (as in batch A). (b) Table showing the fraction of particles observed in each orientation when vitrifying 10 s after spreading of the oil over the water. This table includes all the particles in the acquired images (not just the ones for which a contact angle could be measured accurately) (c) Fractions of batch A particles in each orientation at the interface (blue-tilted (I), red-inverted upright (II), green-upright (III)) as a function of wait time t_w, defined as the time between creating and freezing the interface. The samples at 10 and 60 s have been left standing at ambient conditions, the sample at 6000 s has been immersed in water during the wait to avoid evaporation, and the sample at 600 s has been prepared in both ways and no significant difference can be observed. The data points are averages calculated on each collected image and the error bars are the standard deviations. The total number of particles per each data point is 801 (10 s), 1605 (60 s), 2548 (600 s dry), 1049 (600 s water immersion), and 949 (6000 s), respectively.

3.4 Hierarchy in orientations is preserved over time

We test the robustness of these preferences by varying the wait time, t_w, between the creation of the interface and vitrification. We explore t_w = 10, 60, 600, and 6000 s for batch A. Across all wait times, the hierarchy in preferred orientation remains preserved. Over time, the strong preference for the tilted configuration remains and increases slightly. However, since the relaxation of particle orientation at the interface may be obfuscated by the adsorption of additional particles during the wait period, it is not guaranteed that this distribution represents the steady-state distribution of particle orientations.

To precisely quantify the geometries of each of these configurations, we used the topographical information encoded in the shadows cast during Tungsten coating of the samples. For each spherical lobe, we can determine its radius and contact angle with the interface from its apparent radius and length of its shadow. In configuration I, we can determine the contact angles of each lobe, θ_a and θ_p, as well as the rotation angle, θ_r, describing how the axis of the particle is oriented relative to the surface normal (see Figure 3.3). Histograms for these angles are given in Figure 3.7 for particle batch A vitrified 10 s after interface formation. The means and standard deviations are given in Figure 3.6. I will discuss the column for θ_r theory in the next chapter.

	I					II		III	
particle batch	θ_p [°]	θ_a [°]	θ_r [°] expt	θ_r [°] theory	# p	θ_p [°]	# p	θ_a [°]	# p
A	56 ± 7	91 ± 11	66 ± 7	67 ± 12	216	53 ± 8	75	95 ± 9	11
B	60 ± 8	91 ± 11	66 ± 10	65 ± 12	98	55 ± 8	58	92 ± 15	8
C	65 ± 12	106 ± 11	56 ± 11	51 ± 22	26	65 ± 8	39	100 ± 8	14

Figure 3.6: *The polar and apolar lobes have comparable angles across all three configurations.* Contact angles and rotation angles measured by FreSCa cryo-SEM for sample vitrified 10 s after the interface was created

As a consistency check, we also determined the contact angle of the single exposed

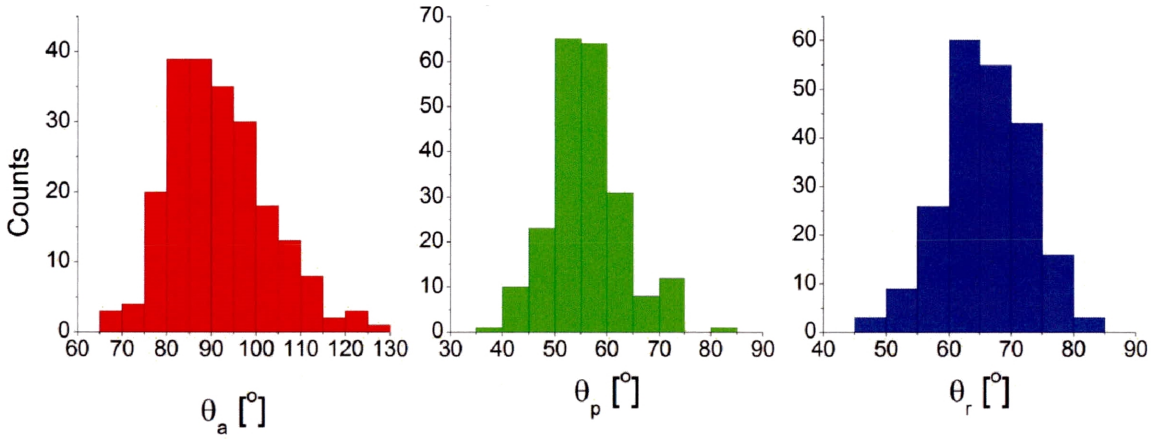

Figure 3.7: *Distribution of angles in Batch A for wait time of 10s.* Contact angles of the (a) apolar lobes and (b) polar lobes. (c) Rotation angles relative to the normal to the interface.

lobe in configurations II and III (refer Figure 3.6). The detailed distributions for the other particle batches are reported in the Supplementary Information of Ref. [39]. These measurements reveal that the particles are slightly amphiphilic. The polar lobes are relatively hydrophilic with contact angles around 60°. The apolar lobes are essentially neutrally wetting, with contact angles slightly larger than 90°. Intriguingly, there is good agreement for the contact angles of each lobe across configurations I, II, and III, refer Figure 3.6. In the tilted configuration I, the long axes of the particles are oriented about 60° from the normal to the interface, as shown in Figure 3.6 and Figure 3.7.

The position and orientations of the particles are steady over time. Through analysis of the shadows cast from the images used to make Figure 3.5 c, we were able to extract the contact angles and rotation angles as a function of time. Figure 3.8 shows the mean and standard deviations of the angles over time based on analysis of particles in configuration I.

Recent work has demonstrated that the contact angles of particles at interfaces may show slow aging, with time scales depending on particle type, size, and geometry. Kaz *et al.* reported logarithmic variations of contact angles over tens and

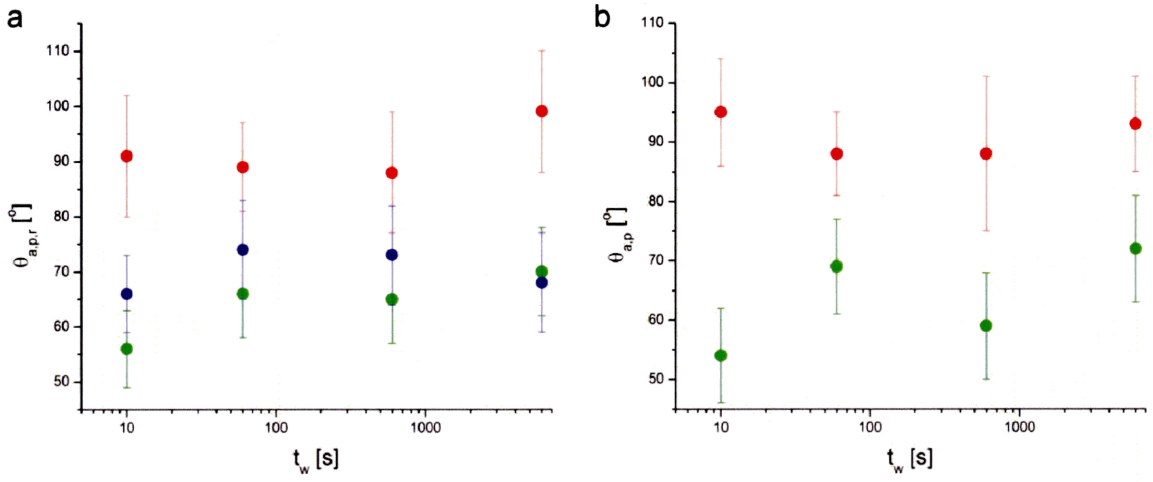

Figure 3.8: *Angles in all three configurations for Batch A particles as a function of wait time.* (a) Contact angles of apolar (red), polar (green) lobes, and rotation angles (blue) for particles in configuration I as a function of wait time. (b) Contact angles of the apolar (red) and polar (green) lobes measured from particles in configuration II and III as a function of wait time.

up to hundreds of seconds for spherical particles [47]. In that work, the particles were placed at the oil/water interface from the water phase using laser tweezers. Recently, Coertjens *et al.* used FreSCa cryo-SEM to show that the contact angles of micrometer-sized ellipsoids display significant variations over the time scale of 1 h [16]. In both cases, the evolution of the contact angles has been attributed to the slow motion of the three-phase contact line over a heterogeneous surface. Such significant variations are not apparent for our dumbbells. We only observe a subtle increase of the contact angle of the polar lobes between 10 and 6000 s; apart from this, no other significant changes are seen over the duration of the experiments.

Chapter 4

Analytical model: adsorption and assembly of dumbbells

A modified version of this chapter was published in *Langmuir* in 2014 [39]. The published work was co-authored with Lucio Isa and Eric R. Dufresne.

4.1 Dumbbells as two overlapping spheres

In equilibrium, the oil/water interface must intersect a particle at an angle determined by the surface energies and surface topography [6, 85]. Since the two lobes have different compositions, the equilibrium contact angle will be different on each lobe. We observe that the contact angle on each lobe is independent of the overall orientation of the particle as shown in Figure 4.1. This observation confirms the dominance of local contact line equilibrium. Since dumbbells are composed of overlapping spherical subunits, the equilibrium condition on both lobes can be satisfied simultaneously with a flat interface. Using simple geometrical arguments, dumbbell orientation can be uniquely determined by the contact angles of each lobe as follows,

$$cos\ \theta_r = \frac{cos\ \theta_p - \alpha\ cos\ \theta_a}{(AR-1)(\alpha+1)} \tag{4.1}$$

4.1.1 Configuration I is an equilibrium state

	I					II		III	
particle batch	θ_r [°]	θ_a [°]	θ_r [°] expt	θ_r [°] theory	# p	θ_r [°]	# p	θ_a [°]	# p
A	56 ± 7	91 ± 11	66 ± 7	67 ± 12	216	53 ± 8	75	95 ± 9	11
B	60 ± 8	91 ± 11	66 ± 10	65 ± 12	98	55 ± 8	58	92 ± 15	8
C	65 ± 12	106 ± 11	56 ± 11	51 ± 22	26	65 ± 8	39	100 ± 8	14

Figure 4.1: *Summary table to compare experimental and predicted angle values.* Contact angles and rotation angles measured by FreSCa cryo-SEM vitrified 10 s after the interface was created.

We use equation 4.1 and the measured values of α, AR, θ_a, and θ_p, from Figure 4.1 to determine the expected dumbbell orientation θ_r. We find excellent agreement with data as shown in Figure 4.1. This simple analytical result is also in agreement with numerical calculations reported in [77, 78] and covers a larger range of α.

The agreement between data and the model makes sense since the governing equations 3.2 and 4.1 assume that particles sit at flat interface. Therefore, our rationale above captures the essence of the mechanisms determining the dumbbell orientation at the oil/water interface.

Deviations from a flat interface can be caused by heterogeneity in the particle shape or chemical functionality and can induce aggregation [76]. However, they do not appear to influence the orientation of our particles at the interface.

Our analysis suggests that the tilted configuration (I) is the equilibrium configuration. We now hypothesize that the single-lobe configurations (II and III), which locally satisfy the contact angle condition, are metastable.

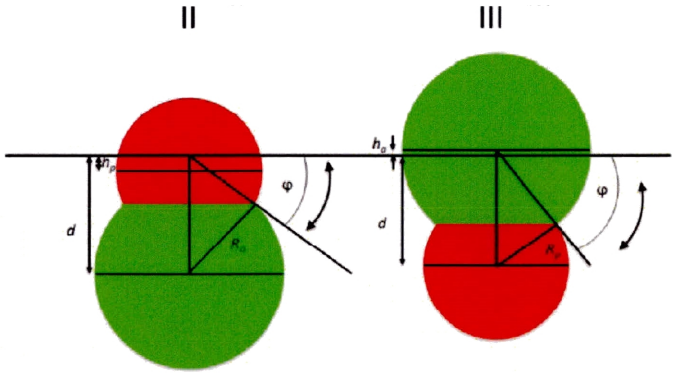

Figure 4.2: *Illustration.* Maximum angle φ required for dumbbells in configurations II and III to relax into configuration I.

4.2 Configurations II and III are metastable states

Configurations II and III are degenerate because many values of θ_r can give the same θ_a and θ_p. For these cases, the second lobe can *snap* into the tilted configuration (lower energy) only by rotational diffusion. However, the time window to do so will be limited if the contact line is pinned on the surface of the lobe. In other words, the particles can remain in these states for much longer before they can rotationally diffuse to achieve a lower energy configuration.

We obtain the upper bounds for metastability of configurations II and III using the following arguments. The farthest away-from-equilibrium θ_r that the particles can be are configurations II and III as represented in Figure 4.2, i.e. the rotation angles are 180° and 0° respectively. In these cases, the dumbbells need to rotate a maximum angle φ before the second lobe can touch the the oil/water interface. For high aspect ratio dumbbells, e.g. AR $\geq$ 1.5, the maximum angles can be calculated as a function of the geometrical quantities and the contact angles of individual lobes as follows,

$$cos\theta_{\varphi} = \frac{\alpha}{(AR-1)(\alpha+1) + cos\ \theta_p} \tag{4.2}$$

$$cos\theta_{\varphi} = \frac{\alpha}{(AR-1)(\alpha+1) - \alpha\ |cos\ \theta_a|} \tag{4.3}$$

Equations 4.2 and 4.3 are for configurations II and III respectively.

Assume that the contact line is fixed on each lobe intersecting the interface in configurations II and III. Then, any rotation around the center of the cross-section at the interface will distort the interface. In turn, interfacial distortion will create a restoring torque to bring the particle to its original position.

The effects of contact line pinning and interfacial distortions have been investigated by Stamou *et al* [94]. We extend their arguments as follows. The distortion of the contact line around a spherical particle is a multipole expansion. For rotation around a pinned contact line, the leading term in the expansion is the dipolar term (the interface dips in the direction of the rotation and rises on the opposite side). As a result, the elastic energy associated with the distortion can be written as,

$$\Delta E \ \approx \ \pi\ \gamma\ (\Delta h)^2 \tag{4.4}$$

where $\Delta\ h$ is the height of the interface deformation.

From Figure 4.2,

$$\Delta h \ \approx \ R_i\ sin\ \theta_i\ sin\ \varphi \tag{4.5}$$

For our dumbbells, we estimate an upper bound on $\Delta E \approx\ 10^5\ k_B T$. This value is high and implies that the lifetime of configurations II and III may be extremely long.

The approximations for the above estimate are an over-representation of reality. Nonetheless, if the contact line is even partially pinned, rotational diffusion of the particle will be significantly hindered due to the high energetic cost involved. Thus, we find the particles *caught in the act* of adsorbing in long-lived states during the preparation and freezing process.

Configuration II, where the polar lobe is attached to the interface, is observed with a higher probability than configuration III where the apolar lobe is in contact with the interface (see Figure 3.5). This may be due to pinning of the contact line on the relatively rougher polar lobes (see Figure 3.1 b). Trapping in metastable orientations due to contact line pinning has been previously reported for larger spherical Janus particles [1]. Contact line pinning may also be suggested by the subtle increase in the contact angle on the polar lobes over time (Figures 3.8).

To summarize, because of this degeneracy, particles in the configurations II and III can only find the interface through rotational diffusion. However, because of the high energetic cost, they should feel no torque driving them to configuration I. Therefore, we expect that the configurations II and III are kinetically trapped and hence, *metastable*.

4.3 Geometric consequences of contact line equilibrium

Particles that sit at the interface with an upright configuration are attractive to the design of particle stabilized emulsions. When particles sit upright, the shape of the particle directly encodes the preferred curvature of the oil/water interface, in a manner analgous to the packing parameter used for molecular surfactants. Equation 4.1 is sufficient to understand the necessary combination of surface chemistry and dumb-

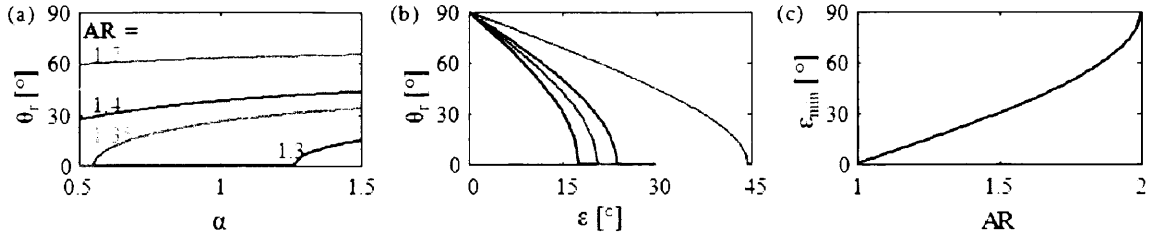

Figure 4.3: *Predictions of analytical model for dumbbell adsorption and assembly at the interface.* (a) Dependence of particle orientation, θ_r, on aspect ratio, AR, and size ratio, α, for experimental values of $\theta_a = 101°$ and $\theta_p = 64°$ in sample. (b) Dependence of θ_r on the contact angles, evaluated by imposing symmetry in wetting of the two lobes, wherein $\theta_a = 90 + \epsilon$ and $\theta_p = 90 - \epsilon$ for given ARs. All angles are in degrees. (c) Minimum ϵ necessary to achieve upright dumbbells for different ARs.

bell shape required to achieve upright packings. In order to achieve upright packings with dumbbells having the same surface compositions explored in the aforementioned experiments, we would need a larger size discrepancy between the two lobes and a much smaller AR than we have been able to achieve with our current synthesis as shown in Figure 4.3 a.

However, upright orientations can also be enforced with a stronger compositional contrast between the two lobes. Let us consider a special case where the contact angles of the apolar and polar are given by $90° \pm \epsilon$. Thus, ϵ quantifies the wetting asymmetry of the particle. In this special case, the relative size of the two lobes, α, conveniently drops out of the expression for θ_r, which now only depends on ϵ and AR. The resulting orientation of the particles as a function of wetting asymmetry is shown in Figure 4.3 b. As the wetting asymmetry increases, the particles stand straighter at the interface. For each aspect ratio, there is a critical value above which the particle stands upright. This critical value increases with the aspect ratio and is plotted in Figure 4.3 c. For AR values that are experimentally accessible to us, we observe a regime of ϵ where the dumbbells prefer the upright orientation. For AR = 1.7, as in batch A, the particles will stand upright for $\theta_a = 135°$ and $\theta_p = 45°$. These contact angle values are not too far off from the reported data in Chapter 3.

4.4 Conclusions

Using FreSCa, we directly visualized and studied the adsorption of individual dumbbells at an oil/water interface. We show that our bulk-synthesized dumbbells have a preferred orientation at the interface and an amphiphilic character, quantified by different contact angles on each lobe. The particles prefer a tilted configuration at the interface, consistent with the equilibrium of a dumbbell with the observed contact angles. Additionally, particles are also trapped in configurations where only one lobe intersects the interface, highlighting a complex adsorption behavior. This study establishes that bulk-synthesized polymer dumbbells can have an amphiphilic nature, but do not currently have sufficient wetting contrast to stand upright at the interface. With improved surface chemistries, bulk-synthesized polymer dumbbells may be a scalable alternative to surface-processed Janus spheres for creating particle surfactants that control the curvature of fluid interfaces.

Chapter 5

Mechanical stability of particle-laden droplets

A modified version of this chapter was published in *Physical Review E* in 2017 [93]. The published work was co-authored with Jin Nam, Raphaël Sarfati, Robert W. Style, and Eric R. Dufresne.

5.1 Introduction

Emulsions are typically produced by the application of shear to immiscible liquids with the help of a surfactant [91]. The mechanical properties of individual emulsion droplets play an important role in determining the rheology of the emulsion [60, 92] and its stability upon the application of further shear, which can be used to trigger the release of encapsulated fluid [68].

The mechanical properties of complex fluid-fluid interfaces are a subject of ongoing investigation [28]. Traditionally, surfactant-laden flat interfaces are characterized under compression using a Langmuir-Blodgett trough. There, the net interfacial ten-

sion, τ, is measured as a function of surface coverage. In the dilute limit, the net interfacial tension is equal to the bare interface tension, γ. As the coverage increases, the adsorbed components interact and resist compression, lowering the net tension [14, 66]. At sufficiently high surface coverage, particle-laden interfaces can have solid-like rheology [28]. As the net tension on the interface vanishes, particle-laden interfaces become unstable and exhibit buckling or corrugation [7].

The mechanics of particle-laden droplets has recently been studied using a variety of approaches [19, 26, 50, 67, 73, 86, 99, 100, 102, 105]. The compression of particle-laden droplets, whose radii are in the vicinity of 10 μm, using Scanning Force Microscopy [26] or Atomic Force Microscopy [99] revealed substantial deviations from the elastic shell models, with apparent contributions from surface tension. The aspiration of sessile particle-laden millimetric droplets observed buckling as the tension of the interface approaches zero [67, 105].

In this chapter, we investigate the mechanics of emulsion droplets using micropipette aspiration. While both particle- and molecule-stabilized droplets are stable, they respond very differently to suction pressure. Droplets stabilized by Sodium Dodecyl Sulfate (SDS) fail at a much lower suction pressure than bare droplets or droplets stabilized with amphiphilic dumbbell particles. While the SDS-stabilized droplets are sucked into the micropipette like a bare droplet, the particle stabilized droplets undergo a two-step failure: first, fluid is removed from the droplet, and then the particle shell buckles. In all cases, however, the magnitude of the critical pressure for these instabilities is set by the fluid surface tension.

5.2 Materials and Methods

5.2.1 Colloidal Particles

We use sub-micron dumbbell-shaped particles as emulsifiers. The largest dimension of the dumbbell particles is 0.5 μm and the lobe radii are 0.25 μm. The particles are weakly amphiphilic with anisotropic wetting preferences at alkane-water interface as described in Chapter 3.

5.2.2 Emulsions

We prepare oil-in-water emulsions by taking 1 mL n-hexadecane and 9 mL of deionized (DI) water in a vial. We gently squirt 0.5 mL of 10% (by weight) particles close to the oil/water interface and vortex the vial immediately for a few seconds. We then use a homogenizer (Ultraturrax T-18) at 10,000 rpm for 60 s to prepare the emulsion. The emulsion is then left to age for three days to ensure that the droplet surfaces are jammed with particles. We repeat this *make-and-wait* protocol for all the emulsion measurements to control for age and extent of surface coverage.

5.2.3 Micropipettes

We prepare micropipettes by pulling glass capillaries (World Precision Instruments TW100-6) in a micropuller (Sutter Instruments P-1000). We then use a microforge (Narshige Instruments MF-900) to cleanly cut the pipettes radii $R_p \in [3,12]$ μm.

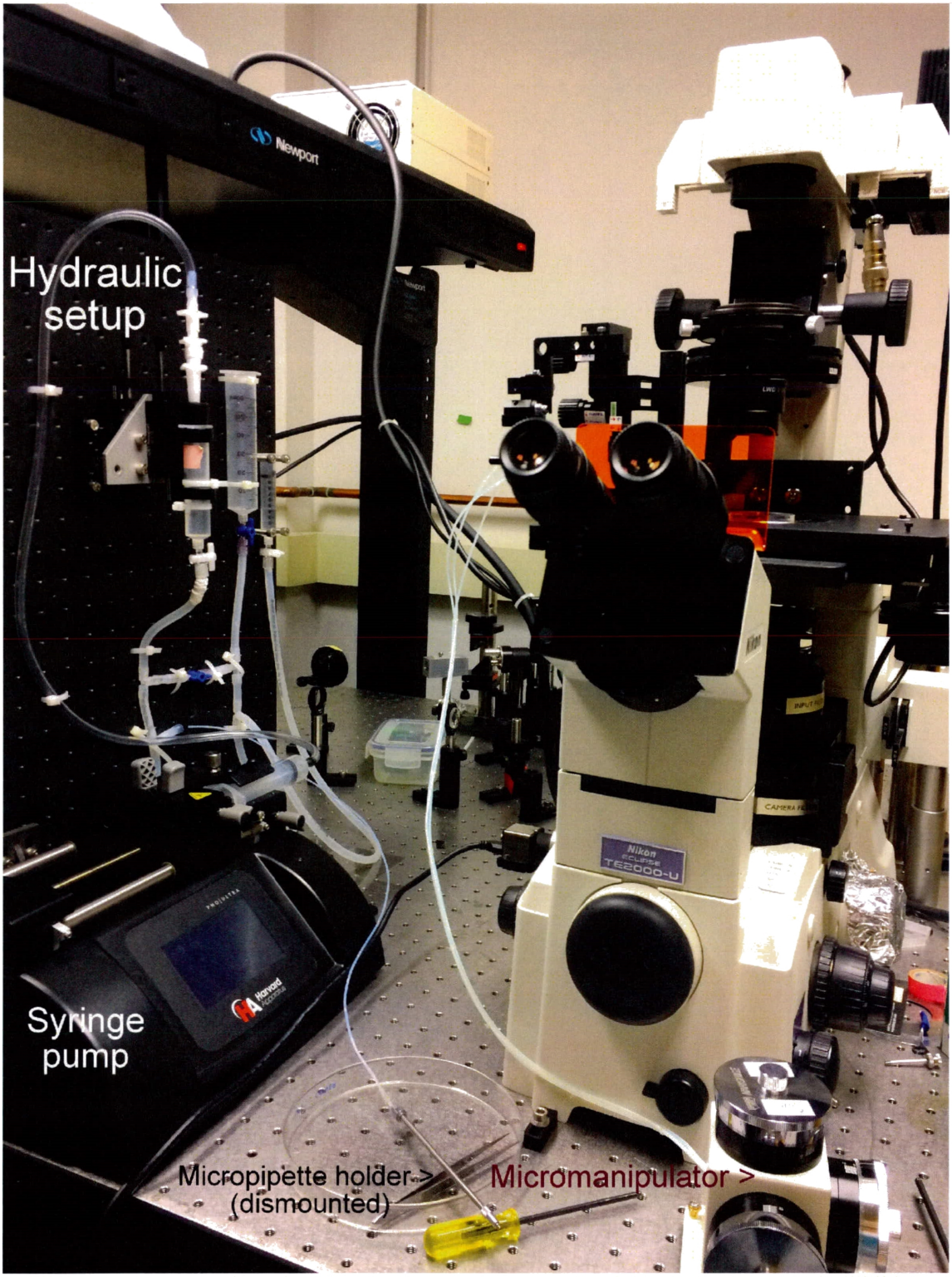

Figure 5.1: *Home-built micropipette aspiration system.* Set-up for micromechanical testing of soft materials including cells and droplets. The pressure in the hydraulic system (labelled) is regulated by controlling the pressure in the gas above the fluid with the aid of a syringe pump (labelled).

5.2.4 Aspiration Setup

We resuspend the buoyant emulsion droplets in a DI water sample chamber for aspiration. The sample is zeroed at atmospheric pressure $P^{(atm)}$. The aspiration setup is shown in Figure 5.1.

On the left is the hydraulic pressure system that is used to apply suction pressure for micropipette aspiration. The set-up consists of three water-filled tubes as shown. where the tube nearest to the syringe pump is used to regulate the pressure and the farther two serve as reservoir and reference respectively. The entire system is initially equilibrated with the sample stage at atmospheric pressure $P^{(atm)}$. We then isolate the reservoir tube (farthest in the picture) and load the micropipette filled with water into the pipette holder (see Figure 5.1) and mount it on the stage. We then isolate the reservoir (middle tube) by closing the valve.

Now, the pressure can be regulated from 0 to 30 kPa below atmosphere with 1 Pa resolution by either controlling the pressure in the gas above the fluid (on the nearest tube) or by moving the height of free surface of the liquid (in that case 1 Pa corresponds to 100 μm). We adopt the first strategy to maximize our range of applicable pressures. We do so by using a syringe pump (Harvard Apparatus 703006) to change the volume of gas above the liquid and regulate the suction pressure (see Figure 5.1). The suction pressure, ΔP, is the difference between the pressure inside the pipette $P^{(pip)}$ and the atmospheric pressure $P^{(atm)}$(where the sample is zero-ed at). ΔP is read out using a pressure transducer (Validyne Engineering P61D-38S) to an accuracy of 0.14 kPa. Note that the pressure transducer is behind the syringe pump and cannot be seen in Figure 5.1.

The micropipette mounted on the stage is connected to a micromanipulator (Figure 5.1, bottom right) that allows us to precisely control the x-, y-, and z-position of

the pipette during the measurement. The micromanipulator is mounted on a larger 3-axis micrometer stage that allows us to position the entire apparatus appropriately for microscopy.

An emulsion droplet is then *gently* aspirated with the micropipette and submerged into DI water to create a uniform environment around the droplet. We then increase the suction pressure using a syringe pump quasi-statically to control for viscosity effects.

5.2.5 Imaging

We track the structural deformation of the droplet in real time using an inverted optical microscope (Nikon Eclipse TE2000-V). We illuminate the sample with a low-N.A. condenser and image using a 40x (N.A. 0.60) air objective. We acquire images at 1 fps for the duration of the experiment using a camera (Thorlabs DC3240M) interfaced with MATLAB.

5.2.6 Analysis

We measure the geometrical parameters, droplet radius R_d and pipette radius R_p, using ImageJ. We capture the images and corresponding pressure reading using Micromanager and MATLAB. We organize and analyze our data using custom codes written in MATLAB.

5.3 Particle-laden droplets exhibit two-step response under aspiration

We study the deformation of particle-laden droplets using micropipette aspiration. Aspiration has been extensively used in biology to investigate the viscoelastic properties of single cells [25,36,44] and cell aggregates [31], stiffness of membranes [3,34,56] and most recently, mechanics of emulsion droplets stabilized by bacteria [45]. The technique allows direct measurement of the mechanical properties of the interface by applying stress locally on the droplets. The stress applied on the droplets can be tuned by changing the differential pressure between the pipette and the ambient environment. Aspiration combined with microscopy enables us to directly visualize the morphological response of droplets in real time and is particularly well-suited for measuring micrometer-scale perturbations [71] .

Gentle aspiration pressures, about 2 kPa, capture droplets at the tip of the micropipette without any visible deformation (see Movie 1 from Supplementary Material of Ref. [93]). Time-lapse imaging over a period of 120 s reveals no rearrangement of the colloidal particles on the droplet surface indicating that the particles have formed a system-spanning solid network on the droplet.

Upon increasing suction, we observe that a small portion of the particle-laden droplet, or *tongue*, is pulled into the pipette. We increase the suction pressure quasi-statically and measure the change in the length of the tongue, Δh. Beyond a pressure threshold, the tongue becomes unstable and continues to grow even when held at constant suction (Figure 5.2 (b)). We call this a *capillary instability* and the corresponding pressure the *critical pressure* given by ΔP_c^{cap} (blue line in Figure 5.2 (b)). The tongue then grows steadily until it pinches off and then re-establishes a new stable tongue length (see Movie 2 from Supplementary Material of Ref. [93]).

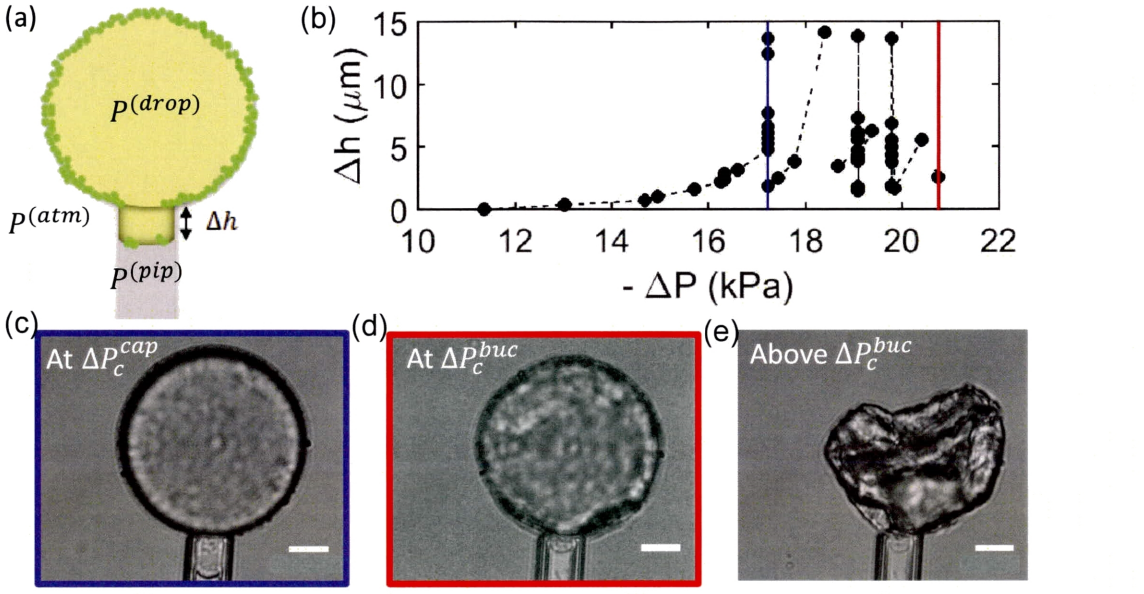

Figure 5.2: *Micropipette aspiration of particle-laden droplets.* (a) Schematic of the experiment. (b) Tongue length, Δh, versus suction pressure, $\Delta P = P^{(pip)} - P^{(atm)}$, which is increased quasi-statically. The dashed line connects data points continuously leading up to pinch off. We identify the onset of capillary instability as the point where Δh grows despite holding the pressure constant, ΔP_c^{cap} *(blue line)*. The droplet eventually buckles at critical pressure ΔP_c^{buc} *(red line)*. (c-e) Images of the droplet (c) at the capillary instability, (d) at the buckling instability, and (e) above the buckling threshold. The scale bar in all images is 15 μm.

In contrast, bare droplets show a catastrophic capillary instability: once the tongue becomes unstable, the bare droplets are entirely sucked into the pipette (see Movie 3 from Supplementary Material of Ref. [93]). Thus, the particles prevent the droplet from being completely sucked into the pipette after the onset of capillary instability.

As the droplet shrinks with further suction, it eventually loses structural symmetry (see Movie 2 from Supplementary Material of Ref. [93]). The morphology of the deformed surface is complex and highly variable. It can develop multiple dimples (Figure 5.3 (a)), large surface folds (Figure 5.3 (b)), or wrinkles (Figure 5.3 (c)). Sometimes, we observe a sudden collapse of the droplet (Figure 5.3 (d)). Upon losing droplet volume or further increase in suction pressure, the surface features grow, eventually leading to the complete collapse of the droplet. We define the suction pressure at this instability point as ΔP_c^{buc} (red line in Figure 5.2 (b)). The variations in the buckling morphology observed likely reflect heterogeneity in the packing

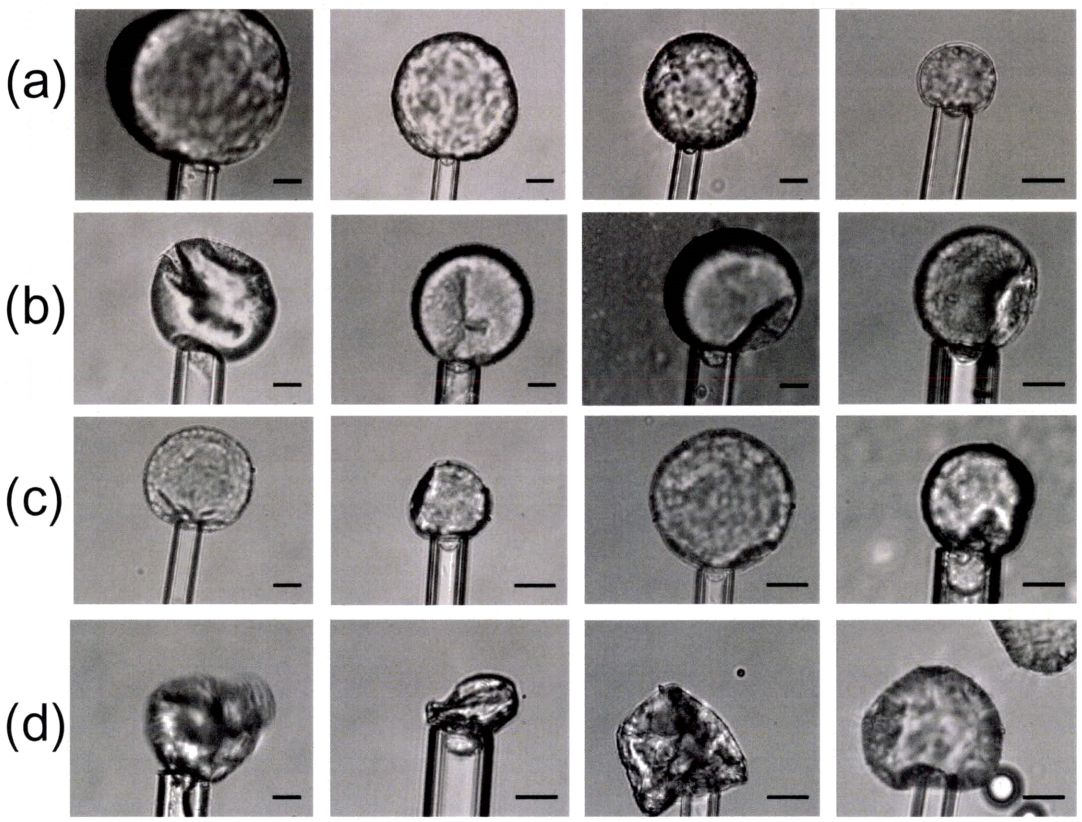

Figure 5.3: *Gallery of elastic instabilities.* At the onset of buckling, we observe surface deformations including (a) multiple dimples, (b) large surface folds, (c) localized wrinkles, and (d) catastrophic failure. The scale bar in all images is 20 μm.

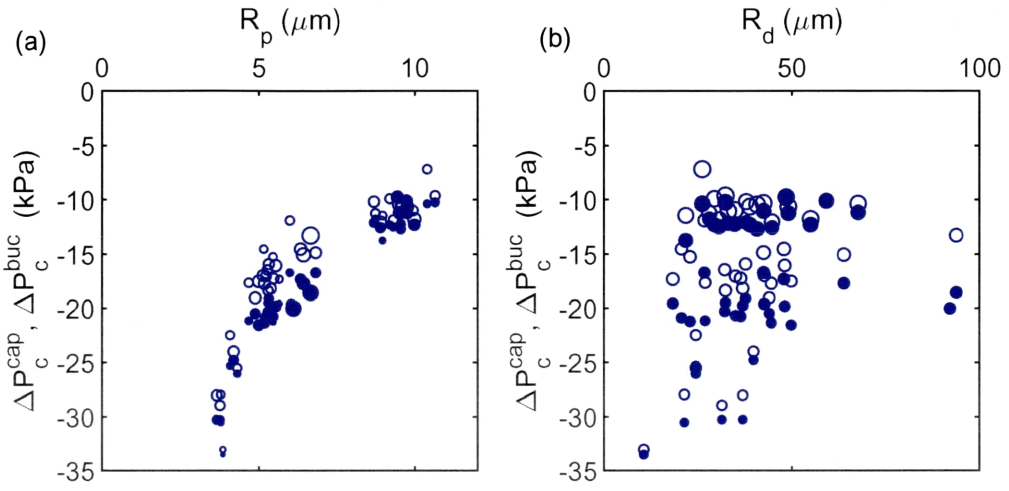

Figure 5.4: *Critical pressure data for particle-laden droplets, varying pipette and droplet radii.* (Left) Critical pressures, ΔP_c^{cap} (open circles) and ΔP_c^{buc} (filled circles) versus pipette radius R_p. Marker size scales with corresponding droplet radius R_d. (Right) The same critical pressures versus R_d. Marker size now scales with corresponding R_p.

of particles on the droplet surface.

The droplet can fully recover its shape upon removing the suction pressure (see Movie 4 from Supplementary Material of Ref. [93]). Upon repeated suction, the shell wrinkles at the same spots (see Movie 4 from Supplementary Material of Ref. [93]). This observation suggests that there are limited particle rearrangements during the course of the droplet deformation, and that the buckling morphology is determined by structural defects in the particle packing.

We have seen that particle-laden droplets fail under suction in two steps: first, a capillary instability, where encapsulated fluid escapes the droplet, and second, an elastic instability, where the shell buckles. To reveal the underlying physics, we measure the onset of these two instabilities as a function of the droplet radius, R_d, and pipette radius, R_p. We vary R_d from 10 - 100 μm and R_p from 3 - 12 μm. Figure 5.4 reports ΔP_c^{cap} with open circles and ΔP_c^{buc} with filled circles for the above range of R_d and R_p. Here, the marker size in the left panel scales with the droplet radius and the marker size in the right panel scales with the pipette radius. While the capillary

instability always precedes buckling, $\Delta P_c^{buc} \leqslant \Delta P_c^{cap}$, both instabilities occur at a similar magnitude of suction, $|\Delta P_c^{buc} - \Delta P_c^{cap}| \ll |\Delta P_c^{cap}|$. The magnitude of the critical pressures decreases strongly with the pipette radius; however, they do not show strong dependence on the droplet size.

5.4 Mechanical equilibrium of fluid interfaces

To understand how this size dependence reflects the mechanical properties of the interface, let us first review the case of a bare droplet. The interface of a bare fluid droplet has a simple state of stress: its tension is independent of shape or deformation, $\tau = \gamma$. Mechanical equilibrium of fluid interfaces is well-captured by the Young- Laplace equation, which states that $\Delta P = \tau\kappa$, where τ is the surface stress and κ is the total interfacial curvature, $2/R$ for a sphere of radius R. Therefore, as the pressure in the pipette is reduced, the curvature of the tongue must increase. However, the curvature of the tongue is limited by the radius of the pipette. Thus, at the limit of mechanical stability [36],

$$\Delta P = P^{(pip)} - P^{(atm)} = 2\tau \left[\frac{1}{R_d} - \frac{1}{R_p} \right]. \tag{5.1}$$

or in terms of the tension,

$$\tau = \frac{\Delta P}{2\ (1/R_d - 1/R_p)}. \tag{5.2}$$

We measured the onset of the capillary instability for a range of bare hexadecane droplets in water. The critical pressure for these droplets shows a clear dependence on the droplet and pipette size (Figure 5.5, green). However, when we use Equation 5.2 and the droplet radius R_d at the onset of capillary instability to calculate the tension, we find that it is independent of R_d or R_p and is $\tau_c = 52.5 \pm 3.1$ mN/m

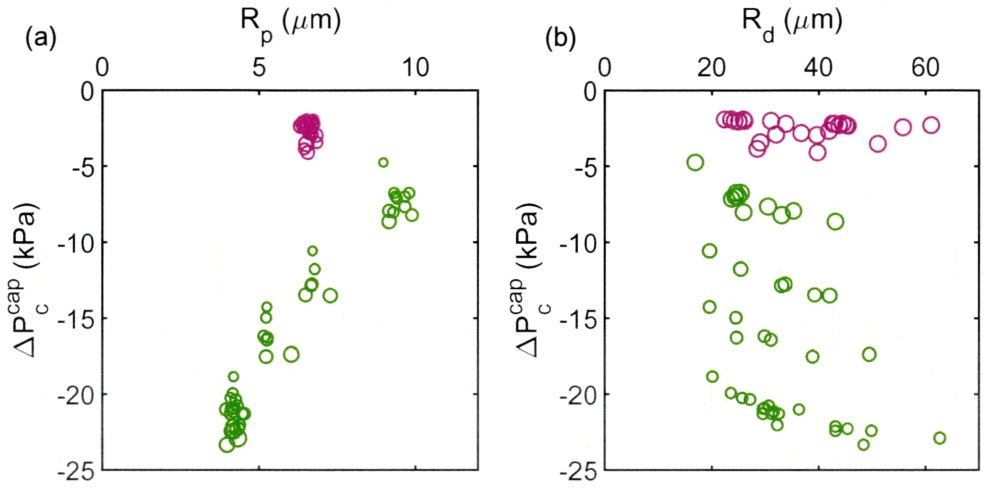

Figure 5.5: *Critical pressure ΔP_c^{cap} for bare droplets (green) and bare droplets in 1% SDS (magenta).* (Left) Critical pressure ΔP_c^{cap} versus pipette radius R_p. Marker size scales with corresponding droplet radius R_d. (Right) The same ΔP_c^{cap} versus R_d. Marker size now scales with corresponding R_p.

(Figure 5.6, green). This is very close to the surface tension of hexadecane/water interface reported in the literature, $\gamma = 53.1$ mN/m [17]. Therefore, the marginal mechanical stability of a bare liquid interface is well described by Equations 5.1 and 5.2 with a constant tension.

For comparison, we prepared hexadecane droplets stabilized in a solution of 1% (by weight) SDS (American Bioanalytical ABO1920-00100), a common molecular surfactant. Upon aspiration, these droplets respond similarly to bare droplets. They undergo a single catastrophic capillary instability without any visible buckling (Figure 5.5, magenta). Like the bare droplet case, we find that the mechanical stability of the droplets is determined by Equations 5.1 and 5.2 with a size-independent tension $\tau_c = 10.2 \pm 2.5$ mN/m (Figure 5.6, magenta). The tension here is much lower than the bare interface case, and is consistent with literature values of the water/SDS/hexadecane surface tension [72]. So although SDS stabilizes the interface, it makes the droplets mechanically weaker and hence, easier to deform.

Given its success in describing the bare and SDS-laden droplets, we apply Equa-

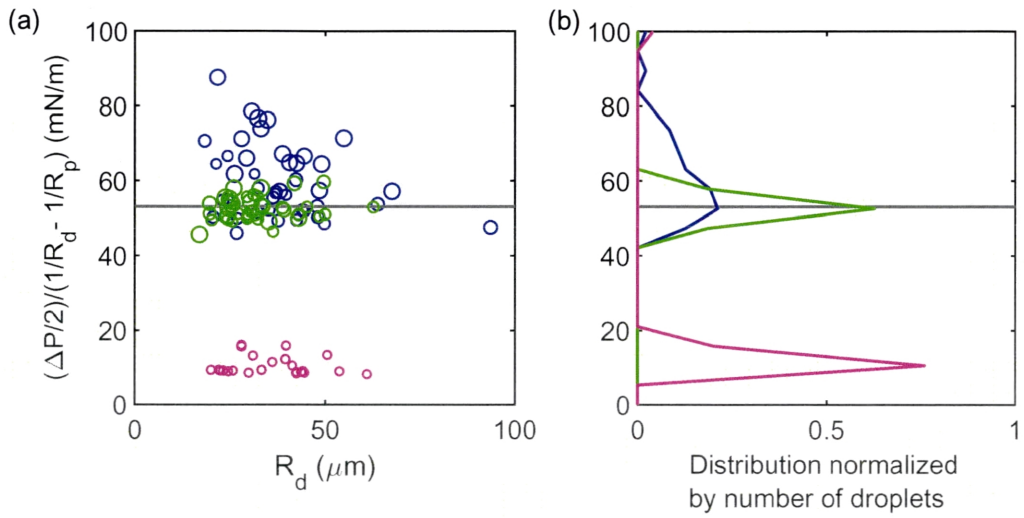

Figure 5.6: *Apparent tension at the onset of the capillary instability, τ_c, based on Laplace equation (5.2) for various droplets.* (Left) τ_c versus droplet radius R_d for particle-laden droplets (blue), bare droplets (green), and bare droplets in 1% SDS (magenta). Solid line is the expected surface tension for a bare droplet, $\gamma = 53.1$ mN/m [17]. (Right) Spread in τ_c normalized by number of droplets.

tion 5.2 to calculate the critical tension for the capillary instability of the particle-laden droplets and plot these results in Figure 5.6; blue. While the largest droplets appear to have a tension similar to the bare droplets, the apparent tension of the smaller droplets is more variable, and greater than or equal to the tension of the bare droplets. This size dependence and the scatter suggests that Equation 5.1 is not appropriate to describe the marginal equilibrium of particle-laden droplets, and that the tension values that Equation 5.2 returns are incorrect.

5.5 Complex stress state for particle-laden droplets under aspiration

Why do Equations 5.1 and 5.2 succeed for bare and SDS-laden droplets while failing for particle-laden droplets? The essential difference lies in the rheology of the interface. While the bare and SDS-laden interfaces are fluid [32], the particle-laden interface is solid. This is a generic feature of particle-laden interfaces at sufficiently

high density [64] [28] and is made apparent in this system by the lack of particle rearrangements at the interface, as described above. For a solid interface, the tension is no longer uniform across the interface, and the state of stress is more complex than assumed in the arguments leading up to Equation 5.1.

We make progress by noting that while aspiration compresses the interface outside the pipette, it dilates the interface inside the pipette. The interface of the tongue should therefore have liquid-like rheology with a tension nearly equal to that of the bare interface. Hence, we can determine the pressure inside the droplet at the point of instability using the Young-Laplace equation, $\Delta P_c^{drop} = \Delta P_c + 2\gamma_{hex-water}/R_p$.

The size dependence of the pressure inside the droplet at the onset of capillary instability, $\Delta P_c^{drop,cap}$, is plotted in Figure 5.7 (top). For bare droplets, shown in green, this pressure increases as the droplet becomes smaller, as predicted by the Young-Laplace equation. However, the pressure inside the particle-laden droplets at the point of capillary instability shows no apparent size dependence and is near zero. The results are very similar if we consider the pressure inside the droplet at the point of buckling, $\Delta P_c^{drop,buc}$, as shown in Figure 5.7 (bottom). Again, we see very little dependence of the pressure on the droplet size, and the values clustered around zero.

The buckling of the particle-laden droplets at zero pressure is consistent with classic observations of surface instabilities of compressed monolayers [7,66,67]. There, it is found that the surface goes unstable when the net tension on the interface approaches zero. The Young-Laplace equation demands that the pressure drop across an interface goes to zero as its tension goes to zero. By that argument, the surface of particle-laden droplets should become unstable when the pressure drop across the interface vanishes. This is consistent with the observed onset of buckling shown in Figure 5.7 (bottom).

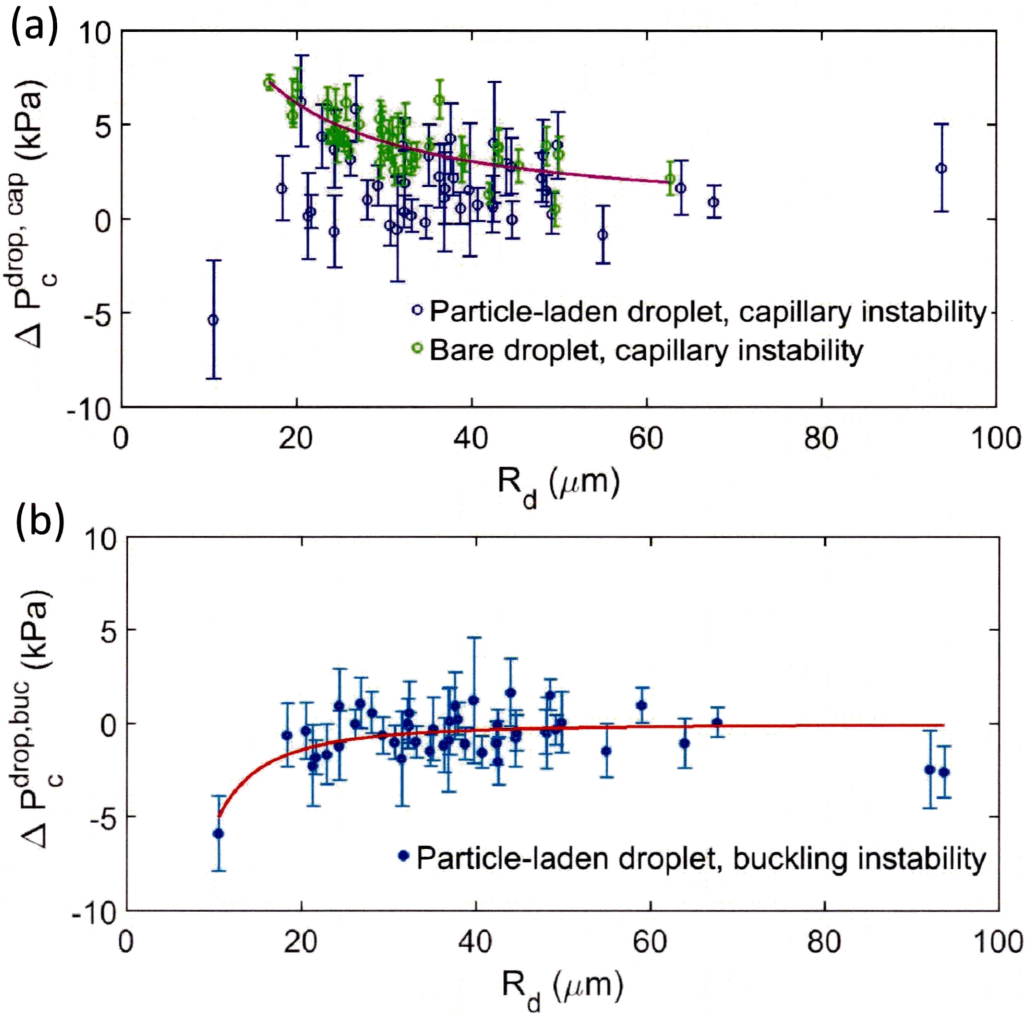

Figure 5.7: *Pressure inside various droplets at the onset of instability.* (Top) $\Delta P_c^{drop,cap}$ at the onset of capillary instability versus droplet radius R_d for particle-laden droplets (blue) and bare droplets (green). The purple line is a Laplace fit and gives $\gamma_{fit} = 58 \pm 1$ mN/m. (Bottom) $\Delta P_c^{drop,buc}$ at the onset of buckling instability. The red curve shows the prediction of Equation 5.3 for $E'.t^2 \leq 560 \pm 1$ kPa $\cdot \mu$m^2.

5.5.1 Predictions from classic thin elastic shell theory

Generally, the vanishing of the tension is insufficient to drive the surface instability since a surface can also have some bending rigidity. The finite rigidity case is captured by the classic linear theory of thin shells [52] [103]. Here, a thin homogeneous linear elastic shell becomes unstable when,

$$\Delta P_c^{drop,buc} = -E' \left(\frac{t}{R_d} \right)^2, \tag{5.3}$$

where t is the shell thickness and E' is a modified Young's modulus, $E' = \frac{E}{\sqrt{3(1-\nu^2)}}$. While the particle shells are inhomogeneous, we use Equation 5.3 to put an upper bound on the apparent value of $E't^2$. The red curve in Figure 5.7 (bottom) shows the prediction of Equation 5.3 for $E't^2 \leq 560$ kPa·μm^2. More precise measurements of the pressure at the onset of buckling would be required to test Equation 5.3 or to provide a reliable value of $E't^2$

5.6 Conclusions

The mechanics of particle-laden droplets was found to be qualitatively different than the mechanics of bare or SDS-stabilized droplets. Particle-laden droplets undergo a two-step failure under suction. First, a capillary instability, where fluid is withdrawn from the shell with minimal change to the droplet shape. Second, an elastic instability, where the shell buckles. Both instabilities occur as the interfacial tension vanishes. The gap in suction pressure between the two instabilities may arise from a finite, but small, bending rigidity of the particle-laden interface. Particle-laden emulsion droplets may be an interesting application of recent advances in our understanding of the far-from-threshold deformation of highly bendable sheets [21, 49, 50].

Chapter 6

Roles of surfactant and ionic strength in the mechanical stability

In the previous chapter, we concluded that surface tension plays a primary role in determining the mechanical stability while shell elasticity only modestly improves it. In this chapter, I aim to independently tune surface tension and shell elasticity to manipulate the onset of mechanical instabilities for the particle-laden droplets.

6.1 Tuning the surface tension of the droplets

I lead experiments with the following question, "How does changing the surface tension of particle-laden droplets change the critical pressures for the onset of mechanical instabilities?"

There are two ways of tuning the interfacial tension for our droplets:

(a) By changing the oil and water combination in the system and formulating new

emulsions with different surface tension γ_{ow}.

(b) By preparing emulsions as described in Chapter 5 and then, shocking them with a molecular surfactant solution right before micropipette aspiration to lower γ_{ow}.

Approach (a) of changing the emulsion formulation poses the risk of changing the preferred contact angles θ_a and θ_p for particles adsorbing to the interface. As a consequence, we might have a different preferred orientation of particles at the interface (θ_r), resulting in a different packing, and hence, different mechanical properties of the droplets. Therefore, we will be changing at least three parameters, namely surface tension γ_{ow}, contact angles θ_a and θ_p, and shell elasticity E', by switching to a different formulation. Hence, option (a) is not ideal for systematic investigations on the role of surface tension in the onset of mechanical stabilities.

Approach (b) of changing surface tension of particle-stabilzed droplets by the adding a molecular surfactant and aspiring right after allows us to significantly lower the surface tension, while preventing the jammed droplets from "equilibrating" to this change. In principle, this approach would change only the surface tension while keeping the interfacial packing consistent with the droplets measured in Chapter 5. Therefore, we will be able to systematically investigate the correspondence between surface tension and the mechanical stability while keeping all other parameters constant.

I proceed with approach (b). Following the *make-and-wait* protocol (see Chapter 5), we prepare hexadecane-in-water emulsions stabilized with dumbbells. After three days, a small fraction of the emulsion droplets are resuspended in a sample chamber containing 1% SDS and aspirated within 1-2 minutes. Unfortunately, the time delay is inevitable and arises from experimental necessities, such as aligning the micropipette and starting data acquisition, before applying suction.

I change the suction pressure quasi-statically as described in the previous chap-

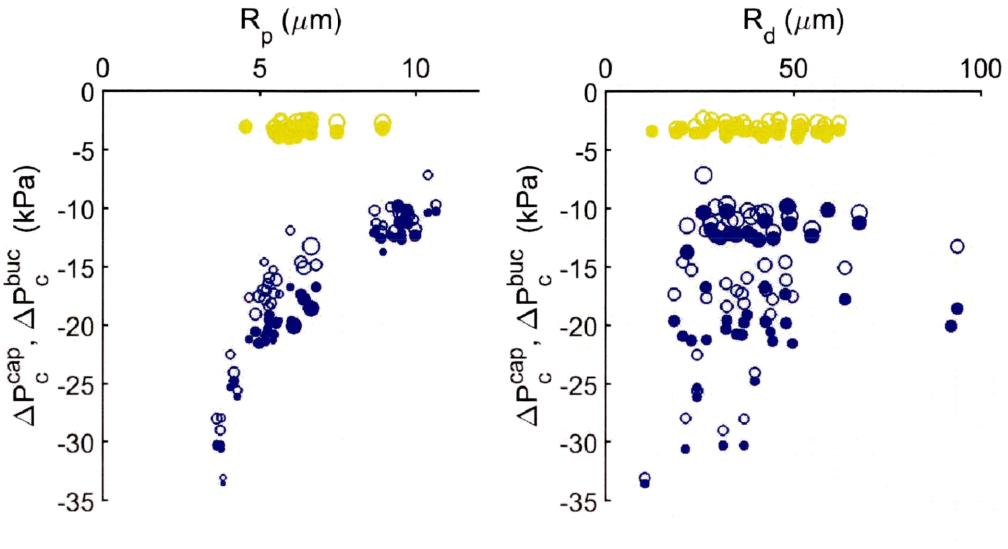

Figure 6.1: *Critical pressure data for particle-laden droplets without SDS (blue) and with SDS (yellow).* (Left) Critical pressures, ΔP_c^{cap} (open circles) and ΔP_c^{buc} (filled circles) versus pipette radius R_p. Marker size scales with corresponding droplet radius R_d. (Right) The same critical pressures versus R_d. Marker size now scales with corresponding R_p.

ter. Recall that particle-laden droplets, without any surfactant, exhibit a two-step response to suctions: first, a capillary instability, where encapsulated fluid escapes the droplet, and second, an elastic instability, where the shell buckles (and can eventually recover its shape upon releasing suction). I measure the onset of these two instabilities as a function of the droplet radius, R_d, and pipette radius, R_p, as reported in Figure 6.1. Open circles are capillary instability, given by ΔP_c^{cap}, and filled circles are buckling instability, given by ΔP_c^{buc}. The marker size in the left panel scales with R_d and the marker size in the right panel scales with the R_p. The blue data are the case of particle-laden droplets without SDS and same as those in Chapter 5, Figure 5.4. The data for particle-laden droplets in SDS are shown in yellow.

The following are some key observations from this data. The droplets exhibit two instability modes: capillary and buckling. This observation suggests that shell is still solid and is further consistent with the movies where I do not see any particles

desorbing from the droplets upon adding SDS. The particle-laden droplets in SDS do not recover their shape upon releasing suction unlike the plain particle-laden droplets (in Chapter 5). Therefore, the structural deformations observed in the presence of SDS may not be *elastic* and could suggest competing interplay between particles and surfactants in re-stabilizing the interface.

The pressure difference between the capillary instability and buckling, i.e. $|\Delta P_c^{buc} - \Delta P_c^{cap}|$ is narrower (Figure 6.1, yellow) when compared to plain particle-laden droplets (Figure 6.1, blue). Aditionally, the droplets become mechanically unstable at much lower suction pressures in the presence of SDS (Figure 6.1, yellow). The critical pressures also do not depend on the droplet and pipette sizes. The pressures are constant and in the same range of magnitude as the bare droplets in SDS (Figure 5.5, magenta). This suggests the dominant role of SDS, or rather, surface tension.

All these findings are different from the typical aspiration data seen for the same emulsion droplets in the absence of a surfactant (Figure 6.1, blue). Nevertheless, the droplets qualitatively exhibit the same modes of instabilities albeit at much lower critical pressures in the presence of SDS. No particles detached from or rearranged at the interface over the course of the experiments.

To better understand the data, I calculate the critical tension at the onset of capillary instability using equation 5.2 described in Chapter 5. Recall from Chapter 5 that bare droplets and bare droplets in 1% SDS exhibit capillary instability at the limit of fluid-fluid surface tension while particle-laden droplets have a much wider spread in the critical tensions, which are all however higher than the bare oil/water surface tension. For the case of particles in 1% SDS, we find that the critical tension (Figure 6.2, yellow) is *same* as that of bare droplets in SDS (Figure 6.2, magenta), $\tau_c = \gamma_{ow/SDS} = 10.5$ mN/m. So, even though paricles stabilize the interface and form a solid shell, evident from buckling modes, the onset of mechanical instabilities

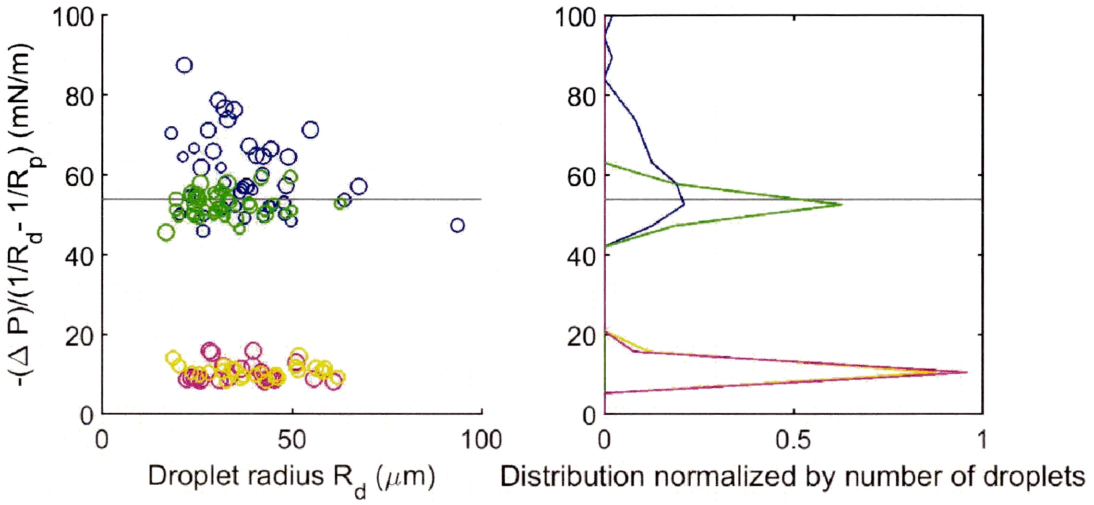

Figure 6.2: *Apparent tension at the onset of the capillary instability, τ_c, based on Laplace equation (5.2) for various droplets.* (Left) τ_c versus droplet radius R_d for particle-laden droplets (blue), bare droplets (green), bare droplets in 1% SDS (magenta), and particle-laden droplets in 1% SDS (yellow). Solid line is the expected surface tension for a bare droplet, $\gamma = 53.1$ mN/m [17]. (Right) Spread in τ_c normalized by number of droplets

is *entirely* determined by the surface tension of the interface. Therefore, surface tension plays a primary role in determining the mechanical stability of particle-laden droplets.

6.2 Tuning shell elasticity with salt and excess particles

The above data leave us with the question, "What are particles adding to the mechanical stability of the droplets apart from introducing two-step response to stress?"

We aim to address this question by independently tuning the elasticity of the solid shell, with a secondary aim of designing tough shells along the way. I do so by introducing salt and excess particles to the particle-laden droplets. The rationale is as follows. The constituent particles are negatively charged at -45 mV according to the zetapotential measurements described in Chapter 2. Adding salt in high con-

centration, in our case 1 M, would screen the charges between the particles allowing them to stick to each other more strongly. As a result, the particulate shells are likely to be thicker, and tougher under stress.

I execute the above concept by taking particle-laden droplets from an emulsion that is three days old and resuspending these droplets in 1 M solution of Sodium Chloride (NaCl) in a vial. I add excess particles, a few μl of 1% by weight, to the droplets in salt solution and gently vortex the vial right away. I let the vial sit for 15 minutes. I then resuspend these droplets in a sample chamber containing 1 M NaCl and aspire on them as soon as possible. Let's call these droplets "salty" droplets for convenience.

Upon aspiration, we observe that the "salty" droplets exhibit a two-stage response to suction pressure, consistent with experiments previously described. The critical pressure data for the onset of instabilities for "salty" droplets are plotted in red in Figure 6.3. The blue data correspond to particle-laden droplets under aspiration as discussed in Chapter 5.

However, this set of preliminary experiments presented several challenges that need to be addressed in future work. Identifying the onset of elastic instability for "salty" droplets is non-trivial due to the rough texture of the droplet surface. The roughness, possibly rising from non-uniformity in thickness of particle layers, makes it difficult to track the shape deformations that mark the onset of elastic instability. As a consequence, the error bars on the critical pressures and corresponding pressure inside the droplet are large, rendering the data ineffectual for measuring shell elasticity. Additionally, the excess particles form a stabilizing network connecting the emulsion droplets making it difficult to isolate individual droplets for aspiration. Nevertheless, the approach is promising to manipulate the shell stiffness and needs careful investigation to identify the exact value of E' as defined in Chapter 5

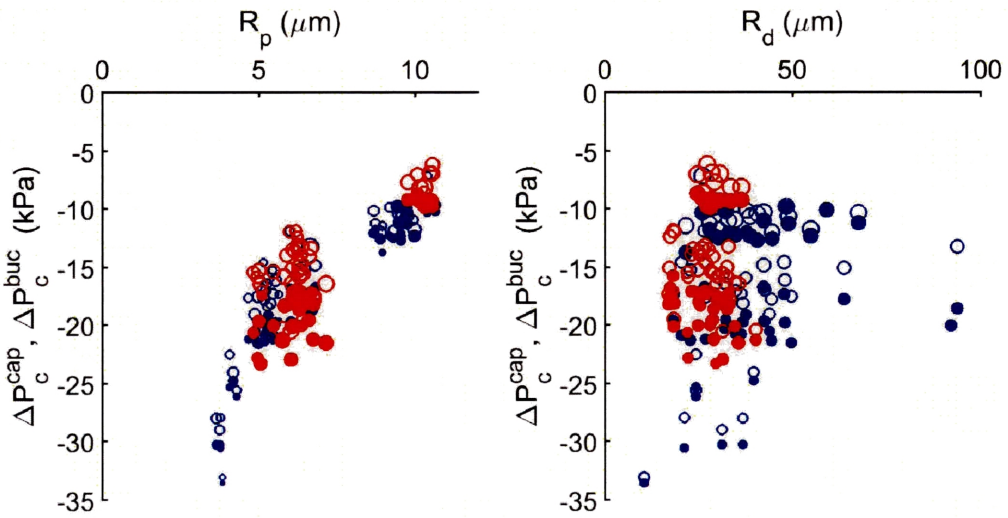

Figure 6.3: *Critical pressure data for particle-laden droplets without salt (blue) and with 1 M NaCl (red).* (Left) Critical pressures, ΔP_c^{cap} (open circles) and ΔP_c^{buc} (filled circles) versus pipette radius R_p. Marker size scales with corresponding droplet radius R_d. (Right) The same critical pressures versus R_d. Marker size now scales with corresponding R_p.

Chapter 7

Conclusions and Outlook

In this thesis, I present dumbbell-shaped nanoparticles as emulsifiers to stabilize oil/water interfaces. Using micropipette aspiration, I discover that dumbbell-laden droplets respond qualitatively differently to stress when compared to bare droplets and bare droplets in molecular surfactant. In all cases, fluid surface tension plays a primary role in determining the mechanical stability of the droplets under micropipette aspiration. While particles dramatically affect the mechanism of failure, their mechanical strength is only modestly improved.

The project opens up new avenues for exploring the structure-property relationship between the dumbbells and the mechanical stability of the assembly on the droplets. The phase space governing the individual particle parameters and emergent mechanical stability needs to be further explored by using different particle types. However, different mechanical assays will be necessary to precisely measure the elastic properties of the particulate shell. Studies connecting the mechanics at the individual droplet level to the bulk rheology of the emulsion would provide the complete mechanical picture across multiple length scales.

Our work is of direct relevance to applications where mechanically-controlled

release of encapsulated fluid makes the droplets functional . Some sectors where our work will be helpful include medicine, personal care products, and food.

Our work is also a novel extension of the ongoing research in mechanics of highly bendable sheets. Specifically, our work is a 3-D extension of the 2-D Lamé Problem currently of interest in the mechanics community [9, 20, 21]. The 2-D Lamé problem is the case of an annular sheet under axisymmetric tensile loads. In this case, there is a mismatch between the planar stresses inside and outside the sheet, resulting in compression, which is relieved through wrinkles. Droplets under aspiration are a 3-D extension, in that the tension on the outside of the droplet is different than the tension inside the pipette. We hope that our work will inspire novel theoretical approaches for solving the Lamé Problem in 3-D, and serve as an experimental complement to theorists working on some classic problems such as wrinkling in pressurized spheres, deformation of soft elastic shells, etc

At the outset, we introduced our dumbbell nanoparticles as colloidal mimics of molecular surfactants. In addition to single particle studies in Chapter 3, we found particles assembled into structures that are closely reminiscent of molecular surfactants. For instance, dumbbells form "micellar" structures as shown in Figure 7.1. The mechanism driving these colloidal assemblies remains unclear and can serve as an exciting domain for future investigation.

Figure 7.1: *Dumbbells form micelle- like structures.*

Bibliography

[1] Dave J Adams, Sarah Adams, John Melrose, and Anthony C Weaver. Influence of particle surface roughness on the behaviour of janus particles at interfaces. *Colloids and Surfaces A: Physicochemical and Engineering Aspects*, 317(1):360–365, 2008.

[2] Shelley Lynn Anna. Droplets and bubbles in microfluidic devices. *Annual Review of Fluid Mechanics*, 48:285–309, 2016.

[3] Takahira Aoki, Toshiro Ohashi, Takeo Matsumoto, and Masaaki Sato. The pipette aspiration applied to the local stiffness measurement of soft tissues. *Annals of biomedical engineering*, 25(3):581–587, 1997.

[4] Samuel O Asekomhe, Raymond Chiang, Jacob H Masliyah, and Janet AW Elliott. Some observations on the contraction behavior of a water-in-oil drop with attached solids. *Industrial & engineering chemistry research*, 44(5):1241–1249, 2005.

[5] Robert Aveyard, Bernard P Binks, and John H Clint. Emulsions stabilised solely by colloidal particles. *Advances in Colloid and Interface Science*, 100:503–546, 2003.

[6] Robert Aveyard and John H Clint. Particle wettability and line tension. *Journal of the Chemical Society, Faraday Transactions*, 92(1):85–89, 1996.

[7] Robert Aveyard, John H Clint, Dieter Nees, and Nick Quirke. Structure and collapse of particle monolayers under lateral pressure at the octane/aqueous surfactant solution interface. *Langmuir*, 16(23):8820–8828, 2000.

[8] James K Beattie, Alex M Djerdjev, and Gregory G Warr. The surface of neat water is basic. *Faraday discussions*, 141:31–39, 2009.

[9] Peter Bella and Robert V Kohn. Wrinkles as the result of compressive stresses in an annular thin film. *Communications on Pure and Applied Mathematics*, 67(5):693–747, 2014.

[10] Bernard P Binks. Particles as surfactantssimilarities and differences. *Current opinion in colloid & interface science*, 7(1):21–41, 2002.

[11] Bernard P. Binks and Tommy S. Hozorov. *Colloidal Particles at Liquid Interfaces*. Cambridge University Press, 2006.

[12] Ned Bowden, Andreas Terfort, Jeff Carbeck, and George M Whitesides. Self-assembly of mesoscale objects into ordered two-dimensional arrays. *Science*, 276(5310):233–235, 1997.

[13] Bastian Brugger, Brian A Rosen, and Walter Richtering. Microgels as stimuli-responsive stabilizers for emulsions. *Langmuir*, 24(21):12202–12208, 2008.

[14] Hans-Jürgen Butt, Karlheinz Graf, and Michael Kappl. *Physics and chemistry of interfaces*. John Wiley & Sons, 2006.

[15] Marcello Cavallaro, Lorenzo Botto, Eric P Lewandowski, Marisa Wang, and Kathleen J Stebe. Curvature-driven capillary migration and assembly of rod-

like particles. *Proceedings of the National Academy of Sciences*, 108(52):20923–20928, 2011.

[16] Stijn Coertjens, Paula Moldenaers, Jan Vermant, and Lucio Isa. Contact angles of microellipsoids at fluid interfaces. *Langmuir*, 30(15):4289–4300, 2014.

[17] AH Cortés-Estrada, LA Ibarra-Bracamontes, A Aguilar-Corona, G Viramontes-Gamboa, and G Carbajal-De la Torre. Surface tension and interfacial tension measurements in water-surfactant-oil systems using pendant drop technique. In *Experimental and Computational Fluid Mechanics*, pages 219–226. Springer, 2014.

[18] Sujit S Datta, Shin-Hyun Kim, Jayson Paulose, Alireza Abbaspourrad, David R Nelson, and David A Weitz. Delayed buckling and guided folding of inhomogeneous capsules. *Physical review letters*, 109(13):134302, 2012.

[19] Sujit S Datta, Ho Cheung Shum, and David A Weitz. Controlled buckling and crumpling of nanoparticle-coated droplets. *Langmuir*, 26(24):18612–18616, 2010.

[20] Benny Davidovitch, Robert D Schroll, and Enrique Cerda. Nonperturbative model for wrinkling in highly bendable sheets. *Physical Review E*, 85(6):066115, 2012.

[21] Benny Davidovitch, Robert D Schroll, Dominic Vella, Mokhtar Adda-Bedia, and Enrique A Cerda. Prototypical model for tensional wrinkling in thin sheets. *Proceedings of the National Academy of Sciences*, 108(45):18227–18232, 2011.

[22] Eric Dickinson. Proteins at interfaces and in emulsions stability, rheology and interactions. *Journal of the Chemical Society, Faraday Transactions*, 94(12):1657–1669, 1998.

[23] Eric Dickinson. Use of nanoparticles and microparticles in the formation and stabilization of food emulsions. *Trends in Food Science & Technology*, 24(1):4–12, 2012.

[24] Dmitry Ershov, Joris Sprakel, Jeroen Appel, Martien A Cohen Stuart, and Jasper van der Gucht. Capillarity-induced ordering of spherical colloids on an interface with anisotropic curvature. *Proceedings of the National Academy of Sciences*, 110(23):9220–9224, 2013.

[25] E Evans and A Yeung. Apparent viscosity and cortical tension of blood granulocytes determined by micropipet aspiration. *Biophysical journal*, 56(1):151–160, 1989.

[26] James K. Ferri, Philippe Carl, Nikolce Gorevski, Thomas P. Russell, Qian Wang, Alexander Böker, and Andreas Fery. Separating membrane and surface tension contributions in pickering droplet deformation. *Soft Matter*, 4:2259 2266, 2008.

[27] Philip Finkle, Hal D Draper, and Joel H Hildebrand. The theory of emulsification1. *Journal of the American Chemical Society*, 45(12):2780 2788, 1923.

[28] Gerald G. Fuller and J. Vermant. Complex fluid-fluid interfaces: rheology and structure. *Annual Review of Chemical and Biomolecular Engineering*, 3:519 543, 2012.

[29] Valeria Garbin, John C Crocker, and Kathleen J Stebe. Nanoparticles at fluid interfaces: Exploiting capping ligands to control adsorption, stability and dynamics. *Journal of colloid and interface science*, 387(1):1–11, 2012.

[30] Bartosz A Grzybowski, Ned Bowden, Francisco Arias, Hong Yang, and George M Whitesides. Modeling of menisci and capillary forces from the mil-

limeter to the micrometer size range. *The Journal of Physical Chemistry B*, 105(2):404–412, 2001.

[31] Karine Guevorkian, Marie-Josée Colbert, Mélanie Durth, Sylvie Dufour, and Françoise Brochard-Wyart. Aspiration of biological viscoelastic drops. *Physical review letters*, 104(21):218101, 2010.

[32] Patrick A Gunning, Andrew R Kirby, Peter J Wilde, Robert Penfold, Nicola C Woodward, and Victor J Morris. Probing the role of interfacial rheology in the relaxation behaviour between deformable oil droplets using force spectroscopy. *Soft Matter*, 9(48):11473–11479, 2013.

[33] Martin F Haase, Kathleen J Stebe, and Daeyeon Lee. Continuous fabrication of hierarchical and asymmetric bijel microparticles, fibers, and membranes by solvent transfer-induced phase separation (strips). *Advanced Materials*, 27(44):7065–7071, 2015.

[34] Jonas Rosager Henriksen and John H Ipsen. Measurement of membrane elasticity by micro-pipette aspiration. *The European Physical Journal E*, 14(2):149 167, 2004.

[35] EM Herzig, KA White, AB Schofield, WCK Poon, and PS Clegg. Bicontinuous emulsions stabilized solely by colloidal particles. *Nature materials*, 6(12):966 971, 2007.

[36] Robert M Hochmuth. Micropipette aspiration of living cells. *Journal of biomechanics*, 33(1):15–22, 2000.

[37] Lucio Isa. Freeze-fracture shadow-casting (fresca) cryo-sem as a tool to investigate the wetting of micro-and nanoparticles at liquid–liquid interfaces. *CHIMIA International Journal for Chemistry*, 67(4):231–235, 2013.

[38] Lucio Isa, Falk Lucas, Roger Wepf, and Erik Reimhult. Measuring single-nanoparticle wetting properties by freeze-fracture shadow-casting cryo-scanning electron microscopy. *Nature communications*, 2:438, 2011.

[39] Lucio Isa, Niveditha Samudrala, and Eric R Dufresne. Adsorption of sub-micron amphiphilic dumbbells to fluid interfaces. *Langmuir*, 30:5057–5063, 2014.

[40] Jacob N Israelachvili. The science and applications of emulsions- an overview. *Colloids and Surfaces A*, 1, 1994.

[41] Jacob N Israelachvili. *Intermolecular and surface forces*. Academic press, 2011.

[42] Kailash C Jena, Rüdiger Scheu, and Sylvie Roke. Surface impurities are not responsible for the charge on the oil/water interface: a comment. *Angewandte Chemie*, 124(52):13112–13114, 2012.

[43] Shan Jiang, Qian Chen, Mukta Tripathy, Erik Luijten, Kenneth S Schweizer, and Steve Granick. Janus particle synthesis and assembly. *Advanced materials*, 22(10):1060–1071, 2010.

[44] Wendy R Jones, H Ping Ting-Beall, Greta M Lee, Scott S Kelley, Robert M Hochmuth, and Farshid Guilak. Alterations in the youngs modulus and volumetric properties of chondrocytes isolated from normal and osteoarthritic human cartilage. *Journal of biomechanics*, 32(2):119–127, 1999.

[45] Zhewen Kang, Anthony Yeung, Julia M. Foght, and Murray R. Gray. Hydrophobic bacteria at the hexadecane-water interface: Examination of micrometer-scale interfacial properties. *Colloids and Surfaces B: Biointerfaces*, 67:59–66, 2008.

[46] Gilad Kaufman, Siamak Nejati, Raphael Sarfati, Rostislav Boltyanskiy, Michael Loewenberg, Eric R. Dufresne, and Chinedum O. Osuji. Soft microcapsules with highly plastic shells formed by interfacial polyelectrolyte-nanoparticle complexation. *Soft Matter*, 11:7478–7482, 2015.

[47] David M Kaz, Ryan McGorty, Madhav Mani, Michael P Brenner, and Vinothan N Manoharan. Physical ageing of the contact line on colloidal particles at liquid interfaces. *Nature materials*, 11(2):138–142, 2012.

[48] Shin-Hyun Kim, Jin-Gyu Park, Tae Min Choi, Vinothan N Manoharan, and David A Weitz. Osmotic-pressure-controlled concentration of colloidal particles in thin-shelled capsules. *Nature communications*, 5, 2014.

[49] Hunter King, Robert D Schroll, Benny Davidovitch, and Narayanan Menon. Elastic sheet on a liquid drop reveals wrinkling and crumpling as distinct symmetry-breaking instabilities. *Proceedings of the National Academy of Sciences*, 109(25):9716–9720, 2012.

[50] Sebastian Knoche, Dominic Vella, Elodie Aumaitre, Patrick Degen, Heinz Rehage, Pietro Cicuta, and Jan Kierfeld. Elastometry of deflated capsules: Elastic moduli from shape and wrinkle analysis. *Langmuir*, 29(40):12463–12471, 2013.

[51] Ankit Kumar, Bum Jun Park, Fuquan Tu, and Daeyeon Lee. Amphiphilic janus particles at fluid interfaces. *Soft Matter*, 9(29):6604–6617, 2013.

[52] Lev D Landau and EM Lifshitz. *Theory of Elasticity, vol. 7*, volume 3. Elsevier, New York, 1986.

[53] Mirjam E Leunissen, Alfons Van Blaaderen, Andrew D Hollingsworth, Matthew T Sullivan, and Paul M Chaikin. Electrostatics at the oil–water

interface, stability, and order in emulsions and colloids. *Proceedings of the National Academy of Sciences*, 104(8):2585–2590, 2007.

[54] Samuel Levine, Bruce D Bowen, and Susan J Partridge. Stabilization of emulsions by fine particles i. partitioning of particles between continuous phase and oil/water interface. *Colloids and Surfaces*, 38(2):325–343, 1989.

[55] Samuel Levine, Bruce D Bowen, and Susan J Partridge. Stabilization of emulsions by fine particles ii. capillary and van der waals forces between particles. *Colloids and surfaces*, 38(2):345–364, 1989.

[56] Marjorie L Longo and Hung V Ly. Micropipet aspiration for measuring elastic properties of lipid bilayers. *Methods in Membrane Lipids*, pages 421–437, 2007.

[57] Jean-Christophe Loudet, Ahmed M Alsayed, Jian Zhang, and Arjun G Yodh. Capillary interactions between anisotropic colloidal particles. *Physical review letters*, 94(1):018301, 2005.

[58] Vinothan N Manoharan, Mark T Elsesser, and David J Pine. Dense packing and symmetry in small clusters of microspheres. *Science*, 301(5632):483–487, 2003.

[59] Vinothan N Manoharan, Arnout Imhof, James D Thorne, David J Pine, et al. Photonic crystals from emulsion templates. *Advanced Materials*, 13(6):447–450, 2001.

[60] Thomas G. Mason, J. Bibette, and David A. Weitz. Yielding and flow of monodisperse emulsions. *Journal of Colloid and Interfacial Science*, 179:439–448, 1996.

[61] David Julian McClements. Protein-stabilized emulsions. *Current opinion in colloid & interface science*, 9(5):305–313, 2004.

[62] Yuan Mei, Guangxian Li, Paula Moldenaers, and Ruth Cardinaels. Dynamics of particle-covered droplets in shear flow: unusual breakup and deformation hysteresis. *Soft Matter*, 12(47):9407–9412, 2016.

[63] Marcel BJ Meinders, William Kloek, and Ton van Vliet. Effect of surface elasticity on ostwald ripening in emulsions. *Langmuir*, 17(13):3923–3929, 2001.

[64] Alma J Mendoza, Eduardo Guzmán, Fernando Martínez-Pedrero, Hernán Ritacco, Ramón G Rubio, Francisco Ortega, Victor M Starov, and Reinhard Miller. Particle laden fluid interfaces: dynamics and interfacial rheology. *Advances in colloid and interface science*, 206:303–319, 2014.

[65] Guangnan Meng, Jayson Paulose, David R Nelson, and Vinothan N Manoharan. Elastic instability of a crystal growing on a curved surface. *Science*, 343(6171):634–637, 2014.

[66] S. Milner, J.F. Joanny, and P. Pincus. Buckling of langmuir monolayers. *Europhysics Letters*, 9:495 – 500, 1989.

[67] Cécile Monteux, John Kirkwood, Hui Xu, Eric Jung, and Gerald G Fuller. Determining the mechanical response of particle-laden fluid interfaces using surface pressure isotherms and bulk pressure measurements of droplets. *Physical Chemistry Chemical Physics*, 9(48):6344–6350, 2007.

[68] V Muguet, M Seiller, G Barratt, O Ozer, JP Marty, and JL Grossiord. Formulation of shear rate sensitive multiple emulsions. *Journal of Controlled Release*, 70(1):37–49, 2001.

[69] Molly K Mulligan and Jonathan P Rothstein. Deformation and breakup of micro-and nanoparticle stabilized droplets in microfluidic extensional flows. *Langmuir*, 27(16):9760–9768, 2011.

[70] Trivikram Nallamilli, Bernard P Binks, Ethayaraja Mani, and Madivala G Basavaraj. Stabilization of pickering emulsions with oppositely charged latex particles: influence of various parameters and particle arrangement around droplets. *Langmuir*, 31(41):11200–11208, 2015.

[71] Martin P Neubauer, Melanie Poehlmann, and Andreas Fery. Microcapsule mechanics: From stability to function. *Advances in colloid and interface science*, 207:65–80, 2014.

[72] S. G. Oh and D. O. Shah. Effect of counterions on the interfacial tension and emulsion droplet size in the oil/water/dodecyl sulfate system. *Journal of Physical Chemistry*, 97:284–286, 1993.

[73] Malika Ouriemi and Petia M Vlahovska. Electrohydrodynamic deformation and rotation of a particle-coated drop. *Langmuir*, 31(23):6298–6305, 2015.

[74] Bum Jun Park, Chang-Hyung Choi, Sung-Min Kang, Kwadwo E Tetteh, Chang-Soo Lee, and Daeyeon Lee. Geometrically and chemically anisotropic particles at an oil–water interface. *Soft Matter*, 9(12):3383–3388, 2013.

[75] Bum Jun Park and Eric M Furst. Fluid-interface templating of two-dimensional colloidal crystals. *Soft Matter*, 6(3):485–488, 2010.

[76] Bum Jun Park and Eric M Furst. Attractive interactions between colloids at the oil–water interface. *Soft Matter*, 7(17):7676–7682, 2011.

[77] Bum Jun Park and Daeyeon Lee. Equilibrium orientation of nonspherical janus particles at fluid–fluid interfaces. *Acs Nano*, 6(1):782–790, 2011.

[78] Bum Jun Park and Daeyeon Lee. Configuration of nonspherical amphiphilic particles at a fluid–fluid interface. *Soft Matter*, 8(29):7690–7698, 2012.

[79] Jin-Gyu Park, Jason D Forster, and Eric R Dufresne. High yield synthesis of monodisperse dumbbell-shaped polymer nanoparticles. *Journal of American Chemical Society*, 132(17):5960–5961, 2010.

[80] L Pauchard, F Parisse, and C Allain. Influence of salt content on crack patterns formed through colloidal suspension desiccation. *Physical Review E*, 59(3):3737, 1999.

[81] Amar B Pawar and Ilona Kretzschmar. Patchy particles by glancing angle deposition. *Langmuir*, 24(2):355–358, 2008.

[82] Amar B Pawar and Ilona Kretzschmar. Multifunctional patchy particles by glancing angle deposition. *Langmuir*, 25(16):9057–9063, 2009.

[83] Adeline Perro, Stéphane Reculusa, Serge Ravaine, Elodie Bourgeat-Lami, and Etienne Duguet. Design and synthesis of janus micro-and nanoparticles. *Journal of materials chemistry*, 15(35-36):3745–3760, 2005.

[84] Spencer U. Pickering. Emulsions. *Journal of the Chemical Society*, 2001, 1907.

[85] Pawel Pieranski. Two-dimensional interfacial colloidal crystals. *Physical Review Letters*, 45(7):569, 1980.

[86] Olivier Pitois, Matthieu Buisson, and Xavier Chateau. On the collapse pressure of armored bubbles and drops. *The European Physical Journal E*, 38(5):1–7, 2015.

[87] W Ramsden. Separation of solids in the surface-layers of solutions and'suspensions'. *Proceedings of the royal Society of London*, 72:156–164, 1903.

[88] Walter Richtering. Responsive emulsions stabilized by stimuli-sensitive microgels: emulsions with special non-pickering properties. *Langmuir*, 28(50):17218–17229, 2012.

[89] Kevin Roger and Bernard Cabane. Uncontaminated hydrophobic/water interfaces are uncharged: a reply. *Angewandte Chemie*, 124(52):13117–13119, 2012.

[90] Kevin Roger and Bernard Cabane. Why are hydrophobic/water interfaces negatively charged? *Angewandte Chemie International Edition*, 51(23):5625–5628, 2012.

[91] Sydney Ross and Ian Douglas Morrison. *Colloidal Dispersions: Suspensions, Emulsions, and Foams*. Wiley, 2002.

[92] Yasushi Saiki, Clive A Prestidge, and Roger G Horn. Effects of droplet deformability on emulsion rheology. *Colloids and Surfaces A: Physicochemical and Engineering Aspects*, 299(1):65–72, 2007.

[93] Niveditha Samudrala, Jin Nam, Raphaël Sarfati, Robert W. Style, and Eric R. Dufresne. Mechanical stability of particle-stabilized droplets under micropipette aspiration. *Physical Review E*, 95:012805, 2017.

[94] Dimitris Stamou, Claus Duschl, and Diethelm Johannsmann. Long-range attraction between colloidal spheres at the air-water interface: The consequence of an irregular meniscus. *Physical Review E*, 62(4):5263, 2000.

[95] Edward J Stancik, Mehrnaz Kouhkan, and Gerald G Fuller. Coalescence of particle-laden fluid interfaces. *Langmuir*, 20(1):90–94, 2004.

[96] Kevin Stratford, Ronojoy Adhikari, Ignacio Pagonabarraga, J-C Desplat, and Michael E Cates. Colloidal jamming at interfaces: A route to fluid-bicontinuous gels. *Science*, 309(5744):2198–2201, 2005.

[97] Yoichi Sugiyama, Ryan J Larsen, Jin-Woong Kim, and David A Weitz. Buckling and crumpling of drying droplets of colloid- polymer suspensions. *Langmuir*, 22(14):6024–6030, 2006.

[98] Nicolas Taccoen, François Lequeux, Deniz Z Gunes, and Charles N Baroud. Probing the mechanical strength of an armored bubble and its implication to particle-stabilized foams. *Physical Review X*, 6(1):011010, 2016.

[99] Sin-Ying Tan, Rico F Tabor, Lydia Ong, Geoffrey W Stevens, and Raymond R Dagastine. Nano-mechanical properties of clay-armoured emulsion droplets. *Soft Matter*, 8(11):3112–3121, 2012.

[100] N Tsapis, ER Dufresne, SS Sinha, CS Riera, JW Hutchinson, L Mahadevan, and DA Weitz. Onset of buckling in drying droplets of colloidal suspensions. *Physical review letters*, 94(1):018302, 2005.

[101] Dominic Vella, P. Aussillous, and L. Mahadevan. Elasticity of an interfacial particle raft. *Europhysics Letters*, 68, 2004.

[102] Petia M Vlahovska. Electrohydrodynamic instabilities of viscous drops. *Physical Review Fluids*, 1(6):060504, 2016.

[103] Th Von Karman and H.S. Tsien. The buckling of spherical shells under external pressure. *Journal of the Aeronautical Sciences*, 7:34 – 42, 1939.

[104] Hongzhi Wang, Virendra Singh, and Sven Holger Behrens. Image charge effects on the formation of pickering emulsions. *The journal of physical chemistry letters*, 3(20):2986–2990, 2012.

[105] Hui Xu, Sonia Melle, Konstantin Golemanov, and Gerald Fuller. Shape and buckling transitions in solid-stabilized drops. *Langmuir*, 21(22):10016–10020, 2005.